HHS Public Access

Author manuscript

Comput Methods Appl Mech Eng. Author manuscript; available in PMC 2019 October 24.

Published in final edited form as:

Comput Methods Appl Mech Eng. 2018 April 1; 331: 23–52. doi:10.1016/j.cma.2017.11.008.

Numerical aspects of anisotropic failure in soft biological tissues favor energy-based criteria: A rate-dependent anisotropic crack phase-field model

Osman Gültekin[a], **Hüsnü Dal**[b], **Gerhard A. Holzapfel**[a,c,*]

[a]Institute of Biomechanics, Graz University of Technology, Stremayrgasse 16/II, 8010, Graz, Austria

[b]Department of Mechanical Engineering, Middle East Technical University, Dumlupınar Bulvarı No. 1, Çankaya, 06800, Ankara, Turkey

[c]Faculty of Engineering Science and Technology, Norwegian University of Science and Technology (NTNU), 7491 Trondheim, Norway

Abstract

A deeper understanding to predict fracture in soft biological tissues is of crucial importance to better guide and improve medical monitoring, planning of surgical interventions and risk assessment of diseases such as aortic dissection, aneurysms, atherosclerosis and tears in tendons and ligaments. In our previous contribution (Gültekin et al., 2016) we have addressed the rupture of aortic tissue by applying a holistic geometrical approach to fracture, namely the crack phase-field approach emanating from variational fracture mechanics and gradient damage theories. In the present study, the crack phase-field model is extended to capture anisotropic fracture using an anisotropic volume-specific crack surface function. In addition, the model is equipped with a rate-dependent formulation of the phase-field evolution. The continuum framework captures anisotropy, is thermodynamically consistent and based on finite strains. The resulting Euler–Lagrange equations are solved by an operator-splitting algorithm on the temporal side which is ensued by a Galerkin-type weak formulation on the spatial side. On the constitutive level, an invariant-based anisotropic material model accommodates the nonlinear elastic response of both the ground matrix and the collagenous components. Subsequently, the basis of extant anisotropic failure criteria are presented with an emphasis on energy-based, Tsai–Wu, Hill, and principal stress criteria. The predictions of the various failure criteria on the crack initiation, and the related crack propagation are studied using representative numerical examples, i.e. a homogeneous problem subjected to uniaxial and planar biaxial deformations is established to demonstrate the corresponding failure surfaces whereas uniaxial extension and peel tests of an anisotropic (hypothetical) tissue deal with the crack propagation with reference to the mentioned failure criteria. Results favor the energy-based criterion as a better candidate to reflect a stable and physically meaningful crack growth, particularly in complex three-dimensional geometries with a highly anisotropic texture at finite strains.

*Corresponding author at: holzapfel@tugraz.at (G.A. Holzapfel).

Keywords

Fracture; Crack phase-field; Failure criteria; Soft biological tissues; Arterial walls; Aorta; Aortic dissection

1. Introduction

The estimation of failure mechanisms in soft biological tissues is of fundamental importance for medical monitoring and preoperative planning of diseases ranging not only from aneurysms (Humphrey and Holzapfel [1] and Kim et al. [2]) to atherosclerosis (Chatzizisis et al. [3] and Holzapfel et al. [4]), but it also pertains to aortic dissection (Criado [5] and Roccabianca et al. [6]) and tears in ligaments and tendons (Lee et al. [7], Weiss and Gardiner [8] and Sharma and Maffulli [9]). However, the tangled structural composition of soft biological tissues and the gap in our knowledge on the biochemomechanical processes occurring in the tissue at different scales still pose a number of challenges on the modeling endeavors. Besides, the intricate *in vivo* loading conditions impose conspicuous limits on computational models to characterize physically relevant failure. In our previous contribution (Gültekin et al. [10]) we have addressed these issues by establishing a continuum framework within the context of the crack phase-field approach and proposed a novel energy-based anisotropic failure criterion, the linchpin of any fracture model. To date, several contributions have been made with respect to failure criteria, however, to the best of the authors' knowledge, none of them has touched upon the numerical comparisons of failure criteria by embedding them into a finite element formulation at finite strains. In addition, the variety of failure criteria in terms of arguments treated therein (e.g., free-energy functions, stress or strain tensors) makes it necessary to investigate them thoroughly, expose their strengths and weaknesses in terms of their capability to describe an admissible failure surface and a crack propagation which in the end leads to rupture.

Fracture of many materials is preceded and influenced by the progressive occurrence and the interaction of various micro and macro-cracks. Therein included are soft biological tissues which behave anisotropically, a feature originating from the complex collagenous texture embedded in a rather soft isotropic matrix. To elucidate the phenomena of fracture, the strength of materials traditionally provides analytic relations for the failure under combined stresses. Another approach called fracture mechanics regards the failure as a progressive process where the material is assumed to contain flaws for which the size, shape and location determine fracture (Tsai and Hahn [11] and Talreja and Singh [12]). Hill [13] proposed a failure criterion along the lines of von Mises and Huber to account for anisotropic materials, a modification of which was presented by Azzi and Tsai [14], commonly referred to as the Tsai–Hill criterion. The criterion by Tsai and Wu [15] takes different classes of materials into account, thereby conferring a much wider spectrum which ranges from triclinic to isotropic materials. In addition, we refer to two intriguing anisotropic failure criteria proposed mainly for composite laminates, namely the stress-invariant based criterion by Hashin [16] and the strain-energy based criterion by Wolfe and Butalia [17], applied to small strains.

Computational modeling of fracture traditionally deals with the numerical treatment of complex crack topologies, i.e. surface discontinuities. In this regard, numerous contributions have been proposed to date, see, e.g., cohesive element formulations (Ortiz and Pandolfi [18] and Ferrara and Pandolfi [19,20]), element enrichment techniques (Simo et al. [21] and Linder and Armero [22]), nodal enrichment techniques (Belytschko and Black [23], Moës et al. [24] and Gasser and Holzapfel [25]), and energy limiter approaches (Dal and Kaliske [26]), to name but a few. In contrast, the crack phase-field model of fracture avoids the realization of discontinuities and surmounts the well-known shortcomings of the classical theory of brittle fracture by Griffith [27] and Irwin [28], e.g., the determination of curvilinear crack paths and branching angles, as introduced by Francfort and Marigo [29] in the context of a variational principle due to an energy minimization. The numerical implementation of this variational principle conducted by Bourdin et al. [30] approximates the Mumford–Shah functional (Mumford and Shah [31]) with a framework based on the Γ-convergence theory, see Ambrosio and Tortorelli [32]. The key aspect of all these contributions is to provide a diffusive crack topology by smearing out the sharp crack surface over a solid domain regularized by a length-scale parameter l. Recent contributions documented by Miehe and coworkers [33,34] provide a thermodynamically consistent and canonical algorithmic framework for the phase-field formulation for brittle fracture. Extension of these models to dynamic brittle fracture are presented in the studies of Borden et al. [35] and Hofacker and Miehe [36]. The phase-field approach to fracture has hitherto been successfully applied to several coupled multi-physics problems ranging from thermoelastic–plastic to chemomechanical fracture, see, e.g., Miehe et al. [37–39]. Albeit their resemblance of gradient damage theories, crack phase-field models contain the essential ingredients of fracture mechanics such as the critical fracture energy g_c (Griffith-type critical energy release rate), see Griffith [27]. In the meantime, they act as a mediator between the aforementioned approaches, i.e. the strength of materials and the fracture mechanics by bringing them on the same platform.

Based on the extended Cahn–Hilliard model (Cahn and Hilliard [40]), the orientation-dependent crack phase-field evolution has been considered recently by, e.g., Li et al. [41] and Teichtmeister et al. [42] to account for the anisotropic surface energy emanating from the preferred directions in materials. Moreover, Clayton and Knap [43] and Nguyen et al. [44] proposed anisotropic phase-field models for polycrystals. In several materials such as soft biological tissues the anisotropic fracture is not only a geometrical phenomenon but also a mechanical event arisen from the fibrous structure embedded in an otherwise isotropic matrix material which undoubtedly entails the use of an anisotropic crack driving force. Within this context, crack phase-field applications in biomechanics can be found in Gültekin [45], later in Gültekin et al. [10] and Raina and Miehe [46].

The paper is organized as follows. The investigation starts in Section 2 with a brief review of the underlying geometry, kinematics and the constitutive model characterizing an anisotropic elastic response subject to degradation. Subsequently, we pursue a variational principle for the multi-field problem of fracture and obtain the Euler–Lagrange equations based on a power balance. The framework particularly features a viscous extended dissipation functional to account for the rate-dependent evolution of the crack phase-field. Section 3 is then concerned with the theoretical synopsis of the anisotropic failure criteria:

- Energy-based failure criterion
- Tsai–Wu failure criterion
- Hill failure criterion
- Principal stress failure criterion

In Section 4, we employ a staggered solution-update scheme partitioning the monolithic solution into two sub-problems followed by a Galerkin-type weak formulation. Section 5 demonstrates the performance of the proposed model by comparing failure surfaces and crack propagations associated with the above-stated anisotropic failure criteria for simple yet representative boundary-value problems and loading conditions using the finite element analysis. Sections 6 and 7 provide a discussion of the results obtained and a conclusion of the article, respectively.

2. Multi-field problem for failure in anisotropic continuum

We devote this section to phase-field modeling of fracture phenomena. To this end, the primary field variables, namely the crack phase-field d and the deformation map $\boldsymbol{\varphi}$, are introduced in relation to the evolution of the crack and the balance of linear momentum, respectively. Subsequently, an account on constitutive modeling of anisotropic hyperelastic arterial walls consisting of two families of collagen fibers is provided. Afterwards, we report on the saddle point principle of the global power balance due to a quasi-static process of loading, and obtain the Euler– Lagrange equations of the multi-field problem. The numerical edifice, unlike Gültekin [45] and Gültekin et al. [10],also embodies the rate-dependent dissipation functional provided by a Perzyna-type (Perzyna [47]) viscous extension. For the relevant nonlinear continuum mechanics used in the present paper see, e.g., the books and monographs by Eringen [48], Truesdell and Noll [49], Spencer [50], Marsden and Hughes [51], Miehe [52], Holzapfel [53], and Gurtin et al. [54].

2.1. Primary field variables of the multi-field problem

To describe the motion of a solid, we consider a material body at time $t_0 \in \mathcal{T} \subset \mathbb{R}^+$ whose reference configuration possesses an undeformed stress-free state, and is henceforth denoted by $\mathcal{B} \subset \mathbb{R}^3$ with the material point $\mathbf{X} \in \mathcal{B}$, while $\partial\mathcal{B} \subset \mathbb{R}^2$ denotes the surface of the reference configuration $\mathcal{B} \subset \mathbb{R}^3$. The deformed body at current time $t \in \mathcal{T} \subset \mathbb{R}^+$ is then referred to as the spatial configuration designated by $\mathcal{S} \subset \mathbb{R}^3$ with the spatial point $\mathbf{x} \in \mathcal{S}$. The surface of the spatial configuration $\mathcal{S} \subset \mathbb{R}^3$ is expressed by $\partial\mathcal{S} \subset \mathbb{R}^2$ Accordingly, we introduce the bijective deformation map $\boldsymbol{\varphi}(\mathbf{X}, t)$, i.e.

$$\boldsymbol{\varphi}_t(\mathbf{X}): \begin{cases} \mathcal{B} \times \mathcal{T} & \rightarrow \mathcal{S} \\ (\mathbf{X}, t) & \mapsto \mathbf{x} = \boldsymbol{\varphi}(\mathbf{X}, t), \end{cases} \tag{1}$$

which maps a material point **X** onto a spatial point **x**, see Fig. 1. Note that one can also write $\boldsymbol{\varphi}_t(\mathbf{X})$ as long as $t \subset \mathbb{R}^+$ is fixed (Marsden and Hughes [51]). Having characterized the fundamental geometric map for deformations, we can now proceed to the essential geometrical entities of the phase-field modeling. The basic geometric mapping for the time-dependent auxiliary crack phase-field d reads

$$d: \begin{cases} \mathscr{B} \times \mathscr{T} & \rightarrow [0,1], \\ (\mathbf{X}, t) & \mapsto d(\mathbf{X}, t), \end{cases}$$

(2)

which interpolates between the intact ($d = 0$) and the ruptured ($d = 1$) state of the material. The multi-dimensional problem of fracture is basically composed of a deformable mechanical domain and a non-deformable domain of the phase-field, as depicted in Fig. 2(a) and (b), respectively.

2.2. Kinematics

Consider the deformation map $\boldsymbol{\varphi}$ at a fixed time t, then the deformation gradient reads

$$\mathbf{F} = \nabla \boldsymbol{\varphi},$$

(3)

which maps the unit tangent of a reference point onto its counterpart in the spatial configuration. The gradient operators $\nabla(\bullet)$ and $\nabla_x(\bullet)$ denote the gradients with respect to the reference and the spatial coordinates **X** and **x**, respectively. The deformation gradient **F**, its cofactor $\mathrm{cof}\mathbf{F} = J\mathbf{F}^{-\mathrm{T}}$, and its Jacobian $J = \det \mathbf{F}$ relate the deformation of the infinitesimal line (d**X** and d**x**), the area (d**A** and d**a**), and the volume (dV and dv) elements, i.e.

$$\mathrm{d}\mathbf{x} = \mathbf{F}\mathrm{d}\mathbf{X}, \ \mathrm{d}\mathbf{a} = \mathrm{cof}\mathbf{F}\mathrm{d}\mathbf{A}, \ \mathrm{d}v = J\mathrm{d}V.$$

(4)

The deformations are non-penetrable for $J > 0$. Accordingly, we denote the symmetric right and left Cauchy–Green tensors as

$$\mathbf{C} = \mathbf{F}^{\mathrm{T}}\mathbf{g}\mathbf{F},\ \mathbf{b} = \mathbf{F}\mathbf{G}^{-1}\mathbf{F}^{\mathrm{T}},$$

(5)

utilized as deformation measures in the reference and spatial configurations, respectively. Additionally, the continuous three-dimensional manifolds, i.e. the reference configuration $\mathscr{B}$ and the spatial configuration $\mathscr{S}$, are locally equipped with the covariant reference and spatial metric tensors $\mathbf{G} = \delta_{IJ}\mathbf{E}^I \otimes \mathbf{E}^J$ and $\mathbf{g} = \delta_{ij}\mathbf{e}^i \otimes \mathbf{e}^j$, respectively, where δ_{IJ} and δ_{ij} are simply evaluated as the Kronecker deltas. Moreover, the following three invariants

$$I_1 = \mathbf{g}:\mathbf{b},\quad I_2 = \frac{1}{2}\left[I_1^2 - \mathrm{tr}\left(\mathbf{b}^2\right)\right],\quad I_3 = \det\mathbf{b}\,.$$

(6)

account for an isotropic hyperelastic response of a solid in the spatial configuration. The anisotropic mechanical response of the arterial tissue requires the use of additional invariants. To this end, we introduce the Eulerian form of the structure tensors $\mathbf{A}_{\mathbf{m}}$ and $\mathbf{A}_{\mathbf{m}'}$ as

$$\mathbf{A}_{\mathbf{m}} = \mathbf{m} \otimes \mathbf{m},\quad \mathbf{A}_{\mathbf{m}'} = \mathbf{m}' \otimes \mathbf{m}',$$

(7)

where the micro-structure of the tissue is idealized by $\mathbf{m}$ and $\mathbf{m}'$ as the spatial counterparts of the reference unit vectors $\mathbf{M}$ and $\mathbf{M}'$, as shown in Fig. 1. Thus,

$$\mathbf{m} = \mathbf{F}\mathbf{M},\quad \mathbf{m}' = \mathbf{F}\mathbf{M}',$$

(8)

describe two families of fibers embedded in the isotropic ground matrix. Accordingly, we introduce the (physically meaningful) fourth and sixth invariants

$$I_4 = \mathbf{m} \cdot \mathbf{gm}, \quad I_6 = \mathbf{m}' \cdot \mathbf{gm}'$$

(9)

in order to capture the anisotropic response of the tissue.

2.3. Anisotropic crack phase-field model

For a non-deformable domain, the gradient operator can simply be taken as $\nabla_X[\bullet] = \nabla[\bullet]$. Provided that an acute crack surface topology at time t is defined by $\Gamma(t) \subset \mathbb{R}^2$ in the solid $\mathscr{B}$ through a surface integral $\Gamma(d) = \int_\Gamma \mathrm{d}A$, the regularized crack surface $\Gamma_l(d)$ approximated by a volume integral adopts the following three-dimensional form

$$\Gamma_l(d) = \int_{\mathscr{B}} \gamma(d, \nabla d)\mathrm{d}V, \text{ where } \gamma(d, \nabla d) = \frac{1}{2l}\left(d^2 + \nabla d \cdot \nabla d\right)$$

(10)

designates the *isotropic* volume-specific crack surface (crack density) function, which satisfies the condition $\gamma(d, \mathbf{Q} \star \nabla d) = \gamma(d, \nabla d), \forall \mathbf{Q} \in \mathscr{O}(3)$. The tensor variable $\mathbf{Q}$ denotes the rotations in the orthogonal group $\mathscr{O}(3)$, which contains rotations and reflections, and $\star$ stands for the Rayleigh product. The length-scale parameter l controls the breadth of the crack. This approximation can be extended to a class of anisotropic materials such that

$$\Gamma_l(d) = \int_{\mathscr{B}} \gamma(d, \nabla d; \mathscr{L})\mathrm{d}V, \text{ where } \gamma(d, \nabla d; \mathscr{L}) = \frac{1}{2l}\left(d^2 + \nabla d \cdot \mathscr{L} \nabla d\right)$$

(11)

is the *anisotropic* volume-specific crack surface (crack density) function, which satisfies the condition $\gamma(d, \mathbf{Q} \star \nabla d) = \gamma(d, \nabla d), \forall \mathbf{Q} \in \mathscr{G} \subset \mathscr{O}(3)$ where $\mathscr{G}$ designates a symmetry group as a subset of $\mathscr{O}(3)$. The second-order anisotropic structure tensor $\mathscr{L}$ is given as

$$\mathscr{L} = l^2\left[\mathbf{I} + \omega_{\mathbf{M}}(\mathbf{M} \otimes \mathbf{M}) + \omega_{\mathbf{M}'}(\mathbf{M}' \otimes \mathbf{M}')\right],$$

(12)

which aligns the evolution of the crack according to the orientation of fibers in the continuum, see Fig. 3. Therein, the anisotropy parameters ω_{M} and $\omega_{\mathrm{M}'}$ regulate the transition from weak to strong anisotropy for two families of fibers. For isotropic solids, the parameters $\omega_{\mathrm{M}} = \omega_{\mathrm{M}'}$ are zero, whereas for a general anisotropic continuum with several family of fibers, they must lie in an open range, i.e. $-1 < \omega_i < \infty$ where $i \in \{\mathrm{M}, \mathrm{M}', \dots\}$ in order to satisfy the ellipticity condition for $\Gamma_l(d)$. Following this, we can state the minimization principle

$$d(\mathbf{X}, t) = \operatorname{Arg}\left\{ \inf_{d \in \mathscr{W}_{\Gamma(t)}} \Gamma_l(d) \right\}, \tag{13}$$

along with the Dirichlet-type boundary constraint

$$\mathscr{W}_{\Gamma(t)} = \left\{ d \,\middle|\, d(\mathbf{X}, t) = 1 \ \text{ at } \ \mathbf{X} \in \Gamma(t) \right\}. \tag{14}$$

Upon the minimization of the regularized crack surface functional we derive the Euler–Lagrange equations according to

$$\frac{1}{l}(d - \nabla d \cdot \mathscr{L} \nabla d) = 0 \text{ in } \mathscr{B}, \quad \text{and} \quad \mathscr{L} \nabla d \cdot \mathbf{N} = 0 \ \text{ on } \partial\mathscr{B}, \tag{15}$$

where the divergence term interpolates d between the intact and the ruptured state of the material. In $(15)_2$ $\mathbf{N}$ denotes the unit surface normal oriented outward in the reference configuration.

2.3.1. The concept of effective length scale—The anisotropic structure tensor $\mathscr{L}$ defined in (12) motivates the concept of *effective* length scale parameter which can be represented by polar plots (Teichtmeister et al. [42]) in the sense of the surface energy $g_c \Gamma_l(d)$ and its reciprocal (Li et al. [41] and Nguyen et al. [44]), where g_c is referred to as the critical fracture energy (Griffith-type critical energy release rate). To this end, imagine the sharp crack $\Gamma \in \mathscr{B}$ to be the parametric curve $\mathbf{X}_\Gamma(\zeta)$ traced out by the parameter ζ, i.e. $\zeta \rightarrow \mathbf{X}_\Gamma(\zeta)$ so that the position of $\forall \mathbf{X} \in \mathscr{B}$ can be uniquely determined by

$$\mathbf{X}(\zeta, v) = \mathbf{X}_{\Gamma}(\zeta) + v\mathbf{e}_{v}\,.$$

(16)

The base vectors $\mathbf{e}_{\zeta}$ and $\mathbf{e}_{v}$ denote the respective unit tangent and the normal at point $\mathbf{X}_{\Gamma}(\zeta)$, and establish the local coordinate system (ζ, v) alongside the global Cartesian system (x, y), see Fig. 4(a). Now, let the angle between the x-axis and the tangent of the crack at position $\mathbf{X}_{\Gamma}(\zeta)$ be $\phi = \angle(\mathbf{e}_{x}, \mathbf{e}_{\zeta})$, while the angle between the orientation $\mathbf{M}$ of a family of fibers and the x-axis is denoted by $\alpha = \angle(\mathbf{e}_{x}, \mathbf{M})$. Then, by assuming the *effective* length scale parameter l_{e} to be sufficiently small compared with the length of the sharp crack $|\Gamma|$ we arrive at

$$l_{\mathrm{e}}(\phi, \alpha) = l^{2}\left[1 + \omega_{\mathrm{M}}\cos(\phi - \alpha) + \omega_{\mathrm{M}'}\sin(\phi - \alpha)\right]$$

(17)

for an orthotropic case, where the second family of fibers $\mathbf{M}'$ is aligned perpendicular to the first fiber family $\mathbf{M}$, see Fig. 4(a).

Fig. 4(b)–(d) depicts the polar plots of the effective length scale parameter $l_{\mathrm{e}}(\phi, \alpha)$, as introduced in (17), for specific choices of ω_{M} and $\omega_{\mathrm{M}'}$. Specifically, the plot denoted by (*) in Fig. 4(c) recovers the transversely isotropic distribution of the effective length scale parameter for $\omega_{\mathrm{M}'} = 0.5$ and vanishing ω_{M}. Another feature of the model is discernable by the plot (**) in Fig. 4(d), where the effective length scale parameter l_{e} renders isotropy with a wider range ($l_{\mathrm{e}} = 1.5l$) for $\omega_{\mathrm{M}} = \omega_{\mathrm{M}'} \equiv 0.5$. This feature is the natural consequence of the second-order phase-field models providing a two-fold symmetry unlike the fourth-order phase-field models conferring a four-fold symmetry, a more detailed discussion can be found in Remark 1.

Remark 1.: A fourth-order crack phase-field approach to fracture has been recently proposed by Borden et al. [55] for isotropic solids. Anisotropic extensions of this fourth-order model are suggested by, e.g., Li et al. [41] and Teichtmeister et al. [42]. In such a case, the anisotropic crack density function in $(11)_2$ can be recast into a more general form, i.e.

$$\gamma\left(d, \nabla d, \nabla^{2} d; \mathscr{L}, \mathbb{L}\right) = \frac{1}{2l}d^{2} + \frac{l}{4}\nabla d \cdot \mathscr{L}\nabla d + \frac{l^{3}}{32}\nabla^{2} d : \mathbb{L} : \nabla^{2} d,$$

(R1.1)

where $\nabla^2 d$ and $\mathbb{L}$ stand for the second gradient of the phase-field and a fourth-order anisotropic structure tensor, respectively. Insertion of (R1.1) into $(11)_1$ together with the minimization principle (13) yields

$$d - \frac{l^2}{2}\nabla d \cdot \mathscr{L}\nabla d + \frac{l^4}{16}\mathrm{Div}\Big[\mathrm{Div}\big(\mathbb{L}\colon \nabla^2 d\big)\Big] = 0, \tag{R1.2}$$

along with the Neumann-type boundary constraints

$$[\mathscr{L}\nabla d + \frac{l^2}{8}\mathrm{Div}\big(\mathbb{L}\colon \nabla^2 d\big)] \cdot \mathbf{N} = 0 \ \text{ on } \partial\mathscr{B}, \quad \text{and} \quad \mathbb{L}\colon \nabla^2 d \cdot \mathbf{N} = \mathbf{0} \ \text{ on } \partial\mathscr{B} \tag{R1.3}$$

The numerical implementation of the above-stated fourth-order approach requires C^1-continuous shape functions for a conforming approximation, an arduous task for 3-dimensional analyses. An account on the alternative treatment circumventing the C^1-continuity requirement is provided by Teichtmeister et al. [42]. Higher-order approaches become particularly relevant for strongly anisotropic materials for which energetically preferable zig-zag crack patterns are observable. However, its relevance to soft biological tissues is dubious as they seem to exhibit weak anisotropy. This is justified by a phenomenon called aortic dissection where the nascent crack in the medial layer of an aorta propagates either axially or helically following the orientation of one fiber family regardless of the existence of other fiber families. Therefore, our modeling endeavors are confined to use a second-order anisotropic crack phase-field approach.

2.4. Constitutive modeling of artery walls

In order to reflect the local anisotropic mechanical behavior of the hypothetically intact arterial wall, we postulate a specific form of the effective Helmholtz free-energy function split into the effective isotropic Ψ_0^{iso} and the anisotropic Ψ_0^{ani} parts,

$$\Psi_0\big(\mathbf{g}, \mathbf{F}, \mathbf{A}_{\mathbf{m}}, \mathbf{A}_{\mathbf{m}'}\big) = \Psi_0^{\mathrm{iso}}(\mathbf{g}, \mathbf{F}, J) + \Psi_0^{\mathrm{ani}}\big(\mathbf{g}, \mathbf{F}, \mathbf{A}_{\mathbf{m}}, \mathbf{A}_{\mathbf{m}'}\big)\,. \tag{18}$$

The effective isotropic part Ψ_0^{iso} and the anisotropic part Ψ_0^{ani} are functions of the invariants such that

$$\Psi_0^{\text{iso}}(\mathbf{g},\mathbf{F},J)=\widehat{\Psi}_0^{\text{iso}}(J,I_1),\quad \Psi_0^{\text{ani}}(\mathbf{g},\mathbf{F},\mathbf{A}_{\text{m}},\mathbf{A}_{\mathbf{m}'})=\widehat{\Psi}_0^{\text{ani}}(I_4,I_6),$$

(19)

for which the following neo-Hookean form

$$\widehat{\Psi}_0^{\text{iso}}(J,I_1)=\kappa(J-\ln J-1)+\frac{\mu}{2}(I_1-2\ln J-3)$$

(20)

represents the mechanical response of the ground matrix, whereas the exponential form

$$\widehat{\Psi}_0^{\text{ani}}(I_4,I_6)=\frac{k_1}{2k_2}\sum_{i=4,6}\left\{\exp[k_2(I_i-1)^2]-1\right\}$$

(21)

represents the elastic response of the two distinct families of collagen fibers (Holzapfel et al. [56]). In (20) κ and μ denote the bulk modulus and the shear modulus, respectively, whereas the anisotropic term (21) involves k_1 and k_2 representing a stress-like material parameter and a dimensionless parameter, respectively. Note that (21) contributes to the mechanical response provided that the concerning family of fibers is under extension, i.e. when $I_4 > 1$ or $I_6 > 1$. To implement the constitutive model in a typical implicit finite element program, we require the stress tensor and its sensitivity with respect to the associated deformation measure. Exploiting the Coleman–Noll procedure on the Clausius–Planck inequality, and using the decoupled form of the effective free energy Ψ_0 in (18), the effective Kirchhoff stress tensor $\boldsymbol{\tau}_0$ is obtained as

$$\boldsymbol{\tau}_0=2\,\partial_{\mathbf{g}}\Psi_0=\boldsymbol{\tau}_0^{\text{iso}}+\boldsymbol{\tau}_0^{\text{ani}}.$$

(22)

The effective Kirchhoff stress $\boldsymbol{\tau}_0$ due to the isotropic and anisotropic contributions, i.e. $\boldsymbol{\tau}_0^{\text{iso}}$ and $\boldsymbol{\tau}_0^{\text{ani}}$, defined in (22), are

$$\boldsymbol{\tau}_0^{\text{iso}} = 2\,\partial_{\mathbf{g}} \Psi_0^{\text{iso}} = \hat{p}\mathbf{g}^{-1} + \mu\left(\mathbf{b} - \mathbf{g}^{-1}\right), \quad \boldsymbol{\tau}_0^{\text{ani}} = 2\,\partial_{\mathbf{g}} \Psi_0^{\text{ani}} = 2\psi_4 \mathbf{m} \otimes \mathbf{m} + 2\psi_6 \mathbf{m}' \otimes \mathbf{m}', \tag{23}$$

where the penalty term reads $\hat{p} = \kappa(J - 1)$. The deformation-dependent scalar coefficients ψ_4 and ψ_6 are defined as

$$\psi_4 = \partial_{I_4} \Psi_0 = k_1 (I_4 - 1) \exp[k_2 (I_4 - 1)^2], \quad \psi_6 = \partial_{I_6} \Psi_0 = k_1 (I_6 - 1) \exp[k_2 (I_6 - 1)^2]. \tag{24}$$

The sensitivity of the effective Kirchhoff stress tensor is established by the spatial elasticity tensor $\mathbb{C}_0$. Thus,

$$\mathbb{C}_0 = 4\,\partial^2_{\mathbf{gg}} \Psi_0 = 2\,\partial_{\mathbf{g}} \boldsymbol{\tau}_0 = \mathbb{C}_0^{\text{iso}} + \mathbb{C}_0^{\text{ani}}, \tag{25}$$

in which the effective elasticity tensor $\mathbb{C}_0^{\text{iso}}$ due to the isotropic part reads

$$\mathbb{C}_0^{\text{iso}} = (\hat{p} + \kappa)\mathbf{g}^{-1} \otimes \mathbf{g}^{-1} - 2(\hat{p} - \mu)\mathbb{I}_{\mathbf{g}^{-1}}. \tag{26}$$

Therein, the symmetric fourth-order identity tensor $\mathbb{I}_{\mathbf{g}^{-1}}$ has the following index form $\left(\mathbb{I}_{\mathbf{g}^{-1}}\right)^{ijkl} = \left(\delta^{ik}\delta^{jl} + \delta^{il}\delta^{jk}\right)/2$. In (25) $\mathbb{C}_0^{\text{ani}}$ describes the anisotropic part of the effective elasticity tensor, which can be expressed as

$$\mathbb{C}_0^{\text{ani}} = 4\psi_{44}\mathbb{M} + 4\psi_{66}\mathbb{M}',$$

(27)

with the scalar coefficients ψ_{44} and ψ_{66} defined as

$$\psi_{44} = \partial_{I_4}\psi_4 = k_1\left[1 + 2k_2(I_4 - 1)^2\right]\exp\left[k_2(I_4 - 1)^2\right],$$
$$\psi_{66} = \partial_{I_6}\psi_6 = k_1\left[1 + 2k_2(I_6 - 1)^2\right]\exp\left[k_2(I_6 - 1)^2\right].$$

(28)

Finally, the fourth-order structure tensors in (27) take on the following forms

$$\mathbb{M} = \mathbf{m}\otimes\mathbf{m}\otimes\mathbf{m}\otimes\mathbf{m}, \quad \mathbb{M}' = \mathbf{m}'\otimes\mathbf{m}'\otimes\mathbf{m}'\otimes\mathbf{m}'.$$

(29)

2.5. Continuous variational formulation based on power balance

This part is concerned with the saddle point principle of the global power balance which yields the coupled Euler–Lagrange equations governing the evolution of the crack phase-field in (i) a rate-independent and (ii) a rate-dependent setting, the balance of linear momentum. We first consider the Helmholtz free-energy function Ψ for a degrading continuum according to

$$\Psi\left(\mathbf{g}, \mathbf{F}, \mathbf{A}_{\mathbf{m}}, \mathbf{A}_{\mathbf{m}'}; d\right) = g(d)\Psi_0\left(\mathbf{g}, \mathbf{F}, \mathbf{A}_{\mathbf{m}}, \mathbf{A}_{\mathbf{m}'}\right),$$

(30)

where Ψ_0 is the effective Helmholtz free-energy function of the hypothetically intact solid according to (18). In (30) the monotonically decreasing quadratic degradation function g has the form

$$g(d) = (1-d)^2 \,. \tag{31}$$

It describes the degradation of the solid/tissue with the evolving crack phase-field parameter d subject to the growth conditions

$$g'(d) \leq 0 \quad \text{with} \quad g(0) = 1, \quad g(1) = 0, \quad g'(1) = 0. \tag{32}$$

The first condition ensures degradation, while the second and third conditions set the limits for the intact and the ruptured state, and the final condition ensures the saturation of $g(d)$ as $d \rightarrow 1$. With this at hand, we can further describe the isotropic and the anisotropic parts of the free-energy function $\Psi = \widehat{\Psi}^{\text{iso}} + \widehat{\Psi}^{\text{ani}}$ for a degrading material, i.e.

$$\widehat{\Psi}^{\text{iso}}\big(J, I_1; d\big) = g(d)\widehat{\Psi}_0^{\text{iso}}\big(J, I_1\big), \quad \widehat{\Psi}^{\text{ani}}\big(I_4, I_6; d\big) = g(d)\widehat{\Psi}_0^{\text{ani}}\big(I_4, I_6\big), \tag{33}$$

respectively. Nevertheless, $g(d)$ may assume an entirely generic form and may be divided into an isotropic and an anisotropic part, as pointed out in Remark 2.

Remark 2.—We hereby present two possible generic forms for the degradation function $g(d)$ in (31) such that

$$g(d) = b\Big[(1-d)^a - (1-d)^{a-1}\Big] + a(1-d)^{a-1} - (a-1)(1-d)^a, \tag{R2.1}$$

as an extension of the cubic degradation function suggested by Borden et al. [57], and

$$g(d) = (1-d)^a, \tag{R2.2}$$

expanding the quadratic form (31). The exponent a and the coefficient b in (R2.1) appear as model and control parameters regulating the softening behavior of the material and the slope of $g(d)$, respectively, see Fig. 5(a)–(c). They are bounded such that $a \geq 2$ and $0 \leq b \leq 2$ to guarantee a monotonic decrease of $g(d)$. The exponent a in (R2.2), however, accepts values $a > 0$ to ensure the monotonic reduction of the bulk response, see Fig. 5(d). The values $a = 3$ and $b = 2$ in (R2.1) retrieves the $g(d)$ used in various crack phase-field models, see, e.g., Bourdin et al. [58] and Miehe et al. [33], whereas $a = 2$ reproduces the same for (R2.2). The classical continuum damage model (Kachanov [59]) is also a special case of (R2.2) for $a = 1$. Fig. 5 reveals the qualitative behavior of the generic form of $g(d)$ due to (R2.1) and (R2.2).

In view of the above-mentioned formalism, distinct degradation functions as to the isotropic and the anisotropic free-energy contributions may become particularly meaningful in soft biological tissues. To this end, we conjecture on (R2.1), i.e.

$$g_{\text{iso}}(d) = b_{\text{iso}}\left[(1-d)^{a_{\text{iso}}} - (1-d)^{a_{\text{iso}}-1}\right] + a_{\text{iso}}(1-d)^{a_{\text{iso}}-1} - (a_{\text{iso}}-1)(1-d)^{a_{\text{iso}}},$$

(R2.3)

and

$$g_{\text{ani}}(d) = b_{\text{ani}}\left[(1-d)^{a_{\text{ani}}} - (1-d)^{a_{\text{ani}}-1}\right] + a_{\text{ani}}(1-d)^{a_{\text{ani}}-1} - (a_{\text{ani}}-1)(1-d)^{a_{\text{ani}}},$$

(R2.4)

which account for the distinct stress softening behavior of the continuum according to the isotropic and anisotropic parameters a_{iso}, b_{iso}, a_{ani}, b_{ani}, respectively. Hence, (R2.2) can be split as follows

$$g_{\text{iso}}(d) = (1-d)^{a_{\text{iso}}} \quad \text{and} \quad g_{\text{ani}}(d) = (1-d)^{a_{\text{ani}}}.$$

(R2.5)

The parameters may be adjusted in accordance with experimental observations which are rather scarce. Since the focus of this manuscript is largely confined to the analysis of anisotropic failure criteria, further insight into the generic degradation functions is spared as a major subject matter for another article.

2.5.1. Rate of energy storage functional in an anisotropic solid and the external power functional: As a point of departure, we define the energy storage functional E of an anisotropic hyperelastic solid as

$$E(\boldsymbol{\varphi}, d) = \int_{\mathscr{B}} \Psi\left(\mathbf{g}, \mathbf{F}, \mathbf{A}_{\mathbf{m}}, \mathbf{A}_{\mathbf{m}'}; d\right) \mathrm{d}V,$$

(34)

by considering the contributions of the free-energy function in (33). The time derivative of (34) gives the rate of energy storage functional $\mathscr{E}$, i.e.

$$\mathscr{E} = \int_{\mathscr{B}} \left(\boldsymbol{\tau} : \mathbf{g} \nabla_x \dot{\boldsymbol{\varphi}} - f \dot{d}\right) \mathrm{d}V,$$

(35)

with the Kirchhoff stress tensor $\boldsymbol{\tau}$ and the energetic force f defined as

$$\boldsymbol{\tau} = g(d)\boldsymbol{\tau}_0, \quad f = -\partial_d \Psi\left(\mathbf{g}, \mathbf{F}, \mathbf{A}_{\mathbf{m}}, \mathbf{A}_{\mathbf{m}'}; d\right),$$

(36)

where $\boldsymbol{\tau}_0$ is expressed in (22). We emphasize that the energetic force f is the work conjugate to d. Subsequently, the external power functional $\mathscr{P}$ can be described as

$$\mathscr{P}(\dot{\boldsymbol{\varphi}}) = \int_{\mathscr{B}} \rho_0 \tilde{\boldsymbol{\gamma}} \cdot \dot{\boldsymbol{\varphi}} \mathrm{d}V + \int_{\partial \mathscr{B}_t} \tilde{\mathbf{t}} \cdot \dot{\boldsymbol{\varphi}} \mathrm{d}a,$$

(37)

Where ρ_0, $\tilde{\boldsymbol{\gamma}}$ and $\tilde{\mathbf{t}}$ represent the material density, the prescribed body force and the spatial surface traction, respectively.

2.5.2. Rate-independent crack dissipation functional with threshold function: To account for the energy dissipated in the continuum, the dissipation functional $\mathscr{D}$ is introduced as

$$\mathscr{D}(\dot{d}) = \int_{\mathscr{B}} g_c \left[\delta_d \gamma(d, \nabla d; \mathscr{L})\right] \dot{d} \, \mathrm{d}V,$$

(38)

where $\delta_d \gamma$ denotes the variational derivative of the anisotropic volume-specific crack surface γ, whereas g_c is referred as the critical fracture energy (Griffith-type critical energy release rate), see Miehe et al. [33] and Gültekin et al. [10]. The second law of thermodynamics strictly demands that the dissipation functional has to be non-negative for all admissible deformation processes ($\mathscr{D} \geq 0$). This thermodynamic inequality is *a priori* fulfilled by a constitutive dissipation function Φ featuring a positive and convex propensity (Miehe [60] and Miehe and Schänzel [61]). This function can readily be stated by the principle of maximum dissipation via the following constrained optimization problem

$$\Phi(\dot{d}; d, \nabla d) = \sup_{\beta \in \mathbb{E}} \beta \dot{d},$$

(39)

which can be solved by a Lagrange method that leads to

$$\Phi(\dot{d}; d, \nabla d) = \sup_{\beta, \lambda \geq 0} \left[\beta \dot{d} - \lambda t_c(\beta; d, \nabla d)\right],$$

(40)

in terms of the local driving force β, dual to $\dot{d}$, and λ is the Lagrange multiplier that enforces the constraint. Additionally, we have defined the threshold function t_c delineating a reversible domain $\mathbb{E}$ such that

$$\mathbb{E}(\beta) = \left\{\beta \in \mathbb{R} \,\middle|\, t_c(\beta; d, \nabla d) = \beta - g_c \left[\delta_d \gamma(d, \nabla d; \mathscr{L})\right] \leq 0\right\}.$$

(41)

Based on (40) the extended dissipation functional $\mathscr{D}_\lambda$ reads

$$\mathscr{D}_{\lambda}(\dot{d}, \beta, \lambda; d) = \int_{\mathscr{B}} \left[\beta \dot{d} - \lambda t_{\mathrm{c}}(\beta; d, \nabla d)\right] \mathrm{d}V \,.$$

(42)

2.5.3. Rate-independent variational formulation based on power balance: A summation of the aforestated functionals (35), (37) and (42) for the description of a rate-type potential Π_{λ} provides the power balance, i.e.

$$\Pi_{\lambda} = \mathscr{E} + \mathscr{D}_{\lambda} - \mathscr{P} \,.$$

(43)

On the basis of the rate-type potential (43), we introduce the saddle point principle for the quasi-static process, i.e.

$$\left\{\dot{\boldsymbol{\varphi}}, \dot{d}, \beta, \lambda\right\} = \mathrm{Arg}\left\{\inf_{\dot{\boldsymbol{\varphi}} \in \mathscr{W}_{\dot{\varphi}}} \inf_{\dot{d} \in \mathscr{W}_{\dot{d}}} \sup_{\beta, \lambda \geq 0} \Pi_{\lambda}\right\},$$

(44)

with the admissible domains for the primary variables

$$\mathscr{W}_{\dot{\varphi}} = \left\{\dot{\boldsymbol{\varphi}} \,\middle|\, \dot{\boldsymbol{\varphi}} = \mathbf{0} \ \text{ on } \ \partial\mathscr{B}_{\varphi}\right\}, \quad \mathscr{W}_{\dot{d}} = \left\{\dot{d} \,\middle|\, \dot{d} = 0 \ \text{ on } \ \partial\mathscr{B}_{d}\right\}.$$

(45)

The variation of the functional Π_{λ} leads to the Euler–Lagrange equations describing the multi-field problem for the rate-independent fracture of an anisotropic hyperelastic solid, i.e.

$$\boxed{\begin{aligned} &1: J\mathrm{div}\left(J^{-1}\boldsymbol{\tau}\right) + \rho_0\tilde{\boldsymbol{\gamma}} = \mathbf{0}, \\ &2: \beta - f = 0, \\ &3: \dot{d} - \lambda = 0 \end{aligned}}$$

(46)

along with the Karush–Kuhn–Tucker-type loading–unloading conditions ensuring the principal of maximum dissipation for the case of an evolution of the crack phase-field parameter d, i.e.

$$\lambda \geq 0, \quad t_{\mathrm{c}} \leq 0, \quad \lambda t_{\mathrm{c}} = 0.$$

(47)

In addition, Neumann-type boundary conditions can be defined as follows

$$J^{-1}\boldsymbol{\tau} \cdot \mathbf{n} = \tilde{\mathbf{t}}, \quad \mathscr{L}\nabla d \cdot \mathbf{N} = 0,$$

(48)

where **n** and **N** represent the unit surface normal oriented outwards in the spatial and the reference configuration, respectively. The elimination of β and λ through $(46)_{2,3}$ and the explicit form of the threshold function t_{c} result in

$$\dot{d} \geq 0, \quad f - g_{\mathrm{c}}\delta_d\gamma(d, \nabla d; \mathscr{L}) \leq 0, \quad \left[f - g_{\mathrm{c}}\delta_d\gamma(d, \nabla d; \mathscr{L})\right]\dot{d} = 0.$$

(49)

The first condition ensures the irreversibility of the evolution of the crack phase-field parameter. The second condition is an equality for an evolving crack, and is negative for a stable crack. The third condition is the balance law for the evolution of the crack phase-field subjected to the former conditions.

2.5.4. Rate-dependent variational formulation based on power balance: The viscous regularization of the rate-independent modality essentially confers stability on the algorithmic setting, a benefit which is purely related to numerics. To this end, we introduce a Perzyna-type (Perzyna [47]) viscous extension of the dissipation functional, i.e.

$$\mathscr{D}_{\eta}(\dot{d},\beta;d)=\int_{\mathscr{B}}[\beta\dot{d}-\frac{1}{2\eta}\langle t_{\mathrm{c}}(\beta;d,\nabla d)\rangle^{2}]\mathrm{d}V,$$

(50)

where the viscosity η determines the viscous over-force governing the evolution of $\dot{d}$. In (50) the positive values for the threshold function t_{c} are always filtered out owing to the ramp function $\langle x\rangle=(x+|x|)/2$. Accordingly, the corresponding viscous rate-type potential reads

$$\Pi_{\eta}=\mathscr{E}+\mathscr{D}_{\eta}-\mathscr{P}.$$

(51)

On the basis of the rate-type potential (51), we propose a viscous extended saddle point principle for the quasi-static process, i.e.

$$\{\dot{\boldsymbol{\varphi}},\dot{d},\beta\}=\mathrm{Arg}\left\{\inf_{\dot{\varphi}\in\mathscr{W}_{\dot{\varphi}}}\inf_{\dot{d}\in\mathscr{W}_{\dot{d}}}\sup_{\beta\geq 0}\Pi_{n}\right\},$$

(52)

with the admissible domains for the primary state variables as given in (45). Evaluating the variation of the potential Π_{η} we obtain the coupled set of Euler–Lagrange equations for the rate-dependent fracture of an anisotropic hyperelastic solid as

$$\boxed{\begin{aligned}&1:J\mathrm{div}\left(J^{-1}\boldsymbol{\tau}\right)+\rho_{0}\tilde{\boldsymbol{\gamma}}=\mathbf{0},\\&2:\beta-f=0,\\&3:\dot{d}-\frac{1}{\eta}\langle t_{\mathrm{c}}(\beta;d,\nabla d)\rangle=0.\end{aligned}}$$

(53)

Substituting f into β, the explicit form of the threshold function t_{c} recasts the equality $(53)_3$ in such a form

$$f = \eta \dot{d} + g_c \delta_d \gamma(d, \nabla d; \mathscr{L}) .$$

(54)

The rate-independent case is recovered for $\eta \to 0$. Note that the Perzyna-type viscous extension transforms the local driving force β such that it becomes unbounded, which enables β to take values outside the domain E in (41). This domain is originally described in elasto-visco-plasticity and continuum damage models, see Miehe [62] and Simo and Hughes [63] among others, and later in the crack phase-field models of Miehe et al. [33] and Miehe and Schänzel [61].

3. Theoretical aspects of anisotropic failure criteria

Focusing on the rate-independent case (54), for $\eta \to 0$, we engage ourselves in building a general framework for the crack phase-field model into which distinct failure criteria can easily be incorporated. We start by elaborating on the energetic force $(36)_2$. Accordingly, we substitute Eqs. (31) and (33) into $(36)_2$ to arrive at

$$f = 2(1 - d)\Psi_0 .$$

(55)

Inserting (55) into (54) for the rate-independent case and adopting $(15)_1$, the following relation holds

$$2(1 - d)\frac{\Psi_0}{g_c/l} = d - \nabla d \cdot \mathscr{L} \nabla d,$$

(56)

whereby one can define the dimensionless crack driving force

$$\boxed{\overline{\mathscr{H}} = \frac{\Psi_0}{g_c/l}},$$

(57)

which already characterizes a criterion for general isotropic materials. Another important feature of (57) is that the dimensionless characteristics of $\overline{\mathscr{H}}$, as discussed by Miehe et al. [37], allows to incorporate different types of failure criteria which we will address in the forthcoming sections. Following this, we stipulate two significant conditions, i.e. the irreversibility of the crack preventing healing effects, and the positiveness of the crack driving force ensuring that the crack growth solely takes place upon loading. Thus,

$$\boxed{\mathscr{H}(t) = \max_{s \in [0,t]} \left[\left\langle \overline{\mathscr{H}}(s) - 1 \right\rangle \right].}$$

(58)

The above ramp-type function is described by the Macaulay brackets which filter out the positive values for $\overline{\mathscr{H}}(s) - 1$ and keeps the solid intact below a threshold value, i.e. until the failure surface is reached; therefore, the crack phase-field does not evolve for $\overline{\mathscr{H}}(s) < 1$. We also note that (58) always takes into account the maximum value of $\overline{\mathscr{H}}(s) - 1$ in the deformation history thereby ensuring the irreversibility of cracking. With these adjustments, (56) now takes on the form

$$\boxed{2(1-d)\mathscr{H} = d - \nabla d \cdot \mathscr{L} \nabla d,}$$

(59)

where the right-hand side of (59) is the geometric resistance to crack whereas the left-hand side is the local source term for the crack growth (Miehe et al. [37]). Bearing this in mind, we recall the rate-dependent case for $\eta \neq 0$, i.e.

$$\boxed{\dot{d} = \frac{1}{\eta}[2(1-d)\mathscr{H} - d + \nabla d \cdot \mathscr{L} \nabla d],}$$

(60)

which compares to (54) with the replacement of the dimensional energetic force by the dimensionless failure Ansatz, the cornerstone of the crack phase-field model. We emphasize that the variational formulation in Section 2 does not apply to cases where stress-based failure criteria are incorporated into the crack phase-field evolution (60). In other words, stress-based criteria, as described in Section 3.2–3.4, can only be added on a rather *ad hoc* basis.

3.1. Energy-based anisotropic failure criterion

The phase-field approach outlined in (53) induces anisotropic failure because of (i) an anisotropic constitutive response and (ii) an anisotropic crack surface energy function. However, the crack driving force $\mathscr{H}$ has a single threshold energy g_c/l for all directions. This is a strong restriction and does not comply with the physically observed phenomenon. In order to characterize anisotropic failure in arterial walls, we have recently proposed a novel energy-based anisotropic failure criterion (Gültekin et al. [10]). This proposed approach is now further elaborated in the present paper.

We start with the assumption that two distinct failure processes governing the cracking of the ground matrix and the fibers, whereby the anisotropic structure tensor $\mathscr{L}$ as introduced in (12), also assumes a distinct form such that

$$\mathscr{L}^{\text{iso}} = l^2\mathbf{I}, \quad \mathscr{L}^{\text{ani}} = l^2\big[\omega_{\text{M}}(\mathbf{M}\otimes\mathbf{M}) + \omega_{\text{M}'}(\mathbf{M}'\otimes\mathbf{M}')\big], \tag{61}$$

which modifies (56) to account for the distinct failure assumption. Thus,

$$f^{\text{iso}} - \frac{g_{\text{c}}^{\text{iso}}}{l}\big(d - \nabla d\cdot\mathscr{L}_{\text{iso}}\nabla d\big) = 0, \quad f^{\text{ani}} - \frac{g_{\text{c}}^{\text{ani}}}{l}\big(d - \nabla d\cdot\mathscr{L}_{\text{ani}}\nabla d\big) = 0. \tag{62}$$

Note that the energetic force f in (55) is additively decomposed into an isotropic part f^{iso} and an anisotropic part f^{ani} such that

$$f^{\text{iso}} = 2(1-d)\widehat{\Psi}_0^{\text{iso}}, \quad f^{\text{ani}} = 2(1-d)\widehat{\Psi}_0^{\text{ani}}. \tag{63}$$

In (62) we have introduced the critical fracture energies over the length scale, namely g_c^{iso}/l for the ground matrix and g_c^{ani}/l for the fibers, which are dual to the effective free-energy functions delineating the isotropic and the anisotropic response, respectively. Insertion of (63) into (62) leads to

$$2(1-d)\frac{\widehat{\Psi}_0^{\mathrm{iso}}}{g_{\mathrm{c}}^{\mathrm{iso}}/l} = d - \nabla d \cdot \mathscr{L}_{\mathrm{iso}} \nabla d, \quad 2(1-d)\frac{\widehat{\Psi}_0^{\mathrm{ani}}}{g_{\mathrm{c}}^{\mathrm{ani}}/l} = d - \nabla d \cdot \mathscr{L}_{\mathrm{ani}} \nabla d\,.$$

(64)

According to the structure of (62) we need to define dimensionless crack driving forces for the isotropic part $\overline{\mathscr{H}}^{\mathrm{iso}}$ and the anisotropic part $\overline{\mathscr{H}}^{\mathrm{ani}}$ such that $\overline{\mathscr{H}} = \overline{\mathscr{H}}^{\mathrm{iso}} + \overline{\mathscr{H}}^{\mathrm{ani}}$. Thus,

$$\overline{\mathscr{H}}^{\mathrm{iso}} = \frac{\widehat{\Psi}_0^{\mathrm{iso}}}{g_{\mathrm{c}}^{\mathrm{iso}}/l}, \quad \overline{\mathscr{H}}^{\mathrm{ani}} = \frac{\widehat{\Psi}_0^{\mathrm{ani}}}{g_{\mathrm{c}}^{\mathrm{ani}}/l}\,.$$

(65)

Superposing the isotropic and anisotropic failure processes (64) with the use of (65), we obtain $(1-d)\overline{\mathscr{H}} = d - (\nabla d \cdot \mathscr{L} \nabla d)/2$. Since $\overline{\mathscr{H}} = \overline{\mathscr{H}}^{\mathrm{iso}} + \overline{\mathscr{H}}^{\mathrm{ani}}$ enters in (58) we can rewrite it as

$$(1-d)\mathscr{H} = d - \frac{1}{2}\nabla d \cdot \mathscr{L} \nabla d,$$

(66)

for the rate-independent case, where the irreversibility of the crack growth is enforced by (58). Without loss of generality, the rate-dependent case can be shown, i.e.

$$\dot{d} = \frac{1}{\eta}\left[(1-d)\mathscr{H} - d + \frac{1}{2}\nabla d \cdot \mathscr{L} \nabla d\right].$$

(67)

The crack phase-field parameter d in (66) and (67) can be considered as a homogenized damage parameter for the anisotropic continuum consisting of matrix and two families of fibers. Nevertheless, one can also envisage n distinct failure processes for the anisotropic part, with n distinct fiber families, i.e. each fiber family may undergo a separate failure process. In that case, the evolution equation for the crack phase-field parameter then reads

$$\dot{d} = \frac{1}{\eta}\left[\frac{2}{n+1}(1-d)\mathscr{H} - d + \frac{1}{n+1}(\nabla d \cdot \mathscr{L}\nabla d)\right], \text{ with } \mathscr{L} = \mathscr{L}^{\text{iso}} + \sum_{i}^{n} \mathscr{L}_i^{\text{ani}}.$$

(68)

3.2. Stress-based anisotropic Tsai–Wu failure criterion

The Tsai–Wu criterion is based on the strength of the material at which the stress space intercepts the assumed failure surface (Tsai and Wu [15]). Accordingly, the dimensionless crack driving force (57) with respect to the effective Cauchy stress tensor $\boldsymbol{\sigma}_0$ assumes the following composition of two scalar functions, i.e.

$$\overline{\mathscr{H}} = \mathbf{T} : \boldsymbol{\sigma}_0 + \boldsymbol{\sigma}_0 : \mathbb{T} : \boldsymbol{\sigma}_0,$$

(69)

where $\mathbf{T}$ denotes a second-order strength tensor while $\mathbb{T}$ is a fourth-order strength tensor. In the crack phase-field model of fracture the crack driving force (69) can easily be incorporated into (58). Note that the principal axes of anisotropy lie on the reference axes – an appropriate transformation can be obtained by rotating the stress components. Through the exploitation of the major and minor symmetries of the strength tensors $\mathbf{T}$ and $\mathbb{T}$ they can be expressed in matrix notation as

$$[\mathbf{T}] = \begin{bmatrix} T_1 \\ T_2 \\ T_3 \\ T_4 \\ T_5 \\ T_6 \end{bmatrix}, \quad [\mathbb{T}] = \begin{bmatrix} T_{11} & T_{12} & T_{13} & T_{14} & T_{15} & T_{16} \\ & T_{22} & T_{23} & T_{24} & T_{25} & T_{26} \\ & & T_{33} & T_{34} & T_{35} & T_{46} \\ & \text{sym} & & T_{44} & T_{45} & T_{56} \\ & & & & T_{55} & T_{56} \\ & & & & & T_{66} \end{bmatrix},$$

(70)

which fall into the triclinic class of material symmetry for a fully anisotropic material. The numbers of independent strength components render 6 and 21, for $(\mathbf{T})_i$ and $(\mathbb{T})_{ij}$, respectively, where $i, j \in \{1 \dots, 6\}$ (Tsai and Wu [15]). Other classes of symmetry relations, e.g., monoclinic, orthotropic, transversely isotropic, cubic and isotropic materials can also be characterized with the help of the strength tensors. In fact, the transformation relations are carried out in accordance with the classical approach to anisotropy, i.e. making use of invariant restrictions to the free-energy function, stress and elasticity tensors.

A particular stability condition is imposed on the strength components of the Tsai–Wu criterion to enforce an ellipsoidal failure surface which necessitates the positive-definiteness of the fourth-order strength tensor such that

$$T_{ii}T_{jj} - T_{ij}^2 \geq 0,$$

(71)

where repeated indices are not summations. In addition, the diagonal terms of the fourth-order strength matrix must be positive so that they become physically meaningful. The symmetry relations endow the model with a feature that causes a number of interaction terms in the fourth-order strength matrix to vanish. As a matter of fact, no interaction exists between the normal/shear components and between the shear/shear components in the off-diagonal terms of the fourth-order strength matrix for an orthotropic material. In particular, the following components would then vanish:

$$T_{14} = T_{24} = T_{34} = T_{15} = T_{25} = T_{35} = T_{45} = T_{16} = T_{26} = T_{36} = T_{46} = T_{56} \equiv 0.$$

(72)

Having identified the simplifications due to symmetry relations, we now proceed to other assumptions which involve further simplifications on the strength matrices [**T**] and [𝕋]. First, it is assumed that the failure strength remains the same due to a change in the sign of the normal or the shear stress which yields

$$T_1 = T_2 = T_3 = T_4 = T_5 = T_6 \equiv 0,$$

(73)

thereby rendering the second-order strength matrix [**T**] obsolete. For a detailed derivation, we refer to Tsai and Wu [15]. This assumption also brings forth the following definition

$$T_{ii} = \frac{1}{\left(\sigma_i^{\mathrm{u}}\right)^2},$$

(74)

for the diagonal terms of the fourth-order strength matrix which are related to the ultimate normal and shear stresses σ_i^{u}, with $i \in \{1, \dots, 6\}$. The off-diagonal terms emanating from the interaction of normal stresses, namely T_{12}, T_{13} and T_{23}, can be ignored, as they are equal to zero, as suggested by Pipes and Cole [64]. On the other hand, Tsai and Hahn [11] proposed an alternative way to identify these terms, i.e.

$$T_{12} = -\sqrt{\frac{T_{11}T_{22}}{4}}, \quad T_{13} = -\sqrt{\frac{T_{11}T_{33}}{4}}, \quad T_{23} = -\sqrt{\frac{T_{22}T_{33}}{4}}.$$

(75)

3.3. Stress-based anisotropic Hill failure criterion

Postulated on the basis of the well-known von Mises–Huber criterion, the anisotropic Hill criterion (Hill [13]) uses the following quadratic form of the dimensionless crack driving force (defined in (57))

$$\overline{\mathscr{H}} = \boldsymbol{\sigma}_0^{\mathrm{vm}} : \mathbb{T} : \boldsymbol{\sigma}_0^{\mathrm{vm}},$$

(76)

where $\boldsymbol{\sigma}_0^{\mathrm{vm}}$ represents the effective von Mises stress tensor. The components of $\boldsymbol{\sigma}_0^{\mathrm{vm}}$ can be defined in terms of general stress components, i.e.

$$\sigma_{0_1}^{\mathrm{vm}} = \sigma_{0_1} - \sigma_{0_2}, \quad \sigma_{0_2}^{\mathrm{vm}} = \sigma_{0_2} - \sigma_{0_3}, \quad \sigma_{0_3}^{\mathrm{vm}} = \sigma_{0_3} - \sigma_{0_1},$$

(77)

for the effective normal stresses. The effective shear stress components of σ_0^{vm} are given as

$$\sigma_{0_4}^{\mathrm{vm}} = \sigma_{0_4}, \quad \sigma_{0_5}^{\mathrm{vm}} = \sigma_{0_5}, \quad \sigma_{0_6}^{\mathrm{vm}} = \sigma_{0_6}.$$

(78)

Note that in (76) the principal axes of anisotropy are chosen to be the reference axes. However, transformations can also be carried out by rotating the stress components. To

characterize the current state of anisotropy, the matrix form of the fourth-order strength tensor T has only non-zero terms in the diagonal, i.e.

$$T_{11} = \frac{1}{2}\left[\frac{1}{\left(\sigma_1^{\mathrm{u}}\right)^2} + \frac{1}{\left(\sigma_2^{\mathrm{u}}\right)^2} - \frac{1}{\left(\sigma_3^{\mathrm{u}}\right)^2}\right],$$
$$T_{22} = \frac{1}{2}\left[\frac{1}{\left(\sigma_2^{\mathrm{u}}\right)^2} + \frac{1}{\left(\sigma_3^{\mathrm{u}}\right)^2} - \frac{1}{\left(\sigma_1^{\mathrm{u}}\right)^2}\right],$$
$$T_{33} = \frac{1}{2}\left[\frac{1}{\left(\sigma_3^{\mathrm{u}}\right)^2} + \frac{1}{\left(\sigma_1^{\mathrm{u}}\right)^2} - \frac{1}{\left(\sigma_2^{\mathrm{u}}\right)^2}\right],$$

(79)

which relate to the effective normal stresses. In addition, (79) accounts for the interactions between the effective normal stresses. The terms connected to the effective shear stresses are given by

$$T_{44} = \frac{1}{4\left(\sigma_4^{\mathrm{u}}\right)^2}, \quad T_{55} = \frac{1}{4\left(\sigma_5^{\mathrm{u}}\right)^2}, \quad T_{66} = \frac{1}{4\left(\sigma_6^{\mathrm{u}}\right)^2}.$$

(80)

Significant features of the Hill criterion are that the failure surface is not necessarily ellipsoidal as no constraint on $\mathbb{T}$ exists, and the failure essentially admits a surface of the von Mises–Huber-type along the isotropic directions.

Remark 3.—It is important to note that in the crack driving forces (69) and (76) the principal axes of anisotropy for the material, say $\{\hat{\mathbf{e}}_1, \hat{\mathbf{e}}_2, \hat{\mathbf{e}}_3\}$, are aligned with the reference basis system, say $\{\mathbf{e}_1, \mathbf{e}_2, \mathbf{e}_2\}$, with the properties

$$\hat{\mathbf{e}}_i \cdot \hat{\mathbf{e}}_j = \delta_{ij} \quad \text{and} \quad \mathbf{e}_i \cdot \mathbf{e}_j = \delta_{ij},$$

(R3.1)

where δ_{ij} denotes the Kronecker delta. In order to apply the mentioned crack driving forces, which are based on the fourth-order strength tensor $\mathbb{T}$, the effective stress tensor $\boldsymbol{\sigma}_0$, obtained according to the reference basis system, needs to be transformed to the material axis, i.e.

$$\hat{\boldsymbol{\sigma}}_0 = \mathbf{Q}\boldsymbol{\sigma}_0\mathbf{Q}^{\mathrm{T}}.$$

(R3.2)

Therein $\mathbf{Q}$ is an orthogonal tensor with the form

$$\mathbf{Q} = Q_{ij}\mathbf{e}_i \otimes \mathbf{e}_j, \quad Q_{ij} = \mathbf{e}_i \cdot \hat{\mathbf{e}}_j,$$

(R3.3)

which transforms the basis system (of analysis) onto the material axis according to

$$\hat{\mathbf{e}}_i = \mathbf{Q}\mathbf{e}_i.$$

(R3.4)

3.4. Principal stress criterion

Developed on the basis of the Rankine theory of failure, the criterion of Raina and Miehe [46] reports on the spectral decomposition of the effective Cauchy stress tensor $\boldsymbol{\sigma}_0$. The authors merely consider the positive principal stresses. Thus,

$$\boldsymbol{\sigma}_0^+ = \sum_{i=1}^{3} \left\langle \sigma_{0_i} \right\rangle \mathbf{n}_i \otimes \mathbf{n}_i,$$

(81)

where σ_{0I} denotes the effective principal stresses, and $\mathbf{n}_I$ are the corresponding eigenvectors for $I \in \{1, 2, 3\}$. Accordingly, the dimensionless crack driving force $\overline{\mathscr{H}}$ in (57) is rewritten as

$$\overline{\mathscr{H}} = \boldsymbol{\sigma}_0^+ : \mathbb{T} : \boldsymbol{\sigma}_0^+,$$

(82)

for which the fourth-order strength tensor $\mathbb{T}$ reads in the index notation

$$(\mathbb{T})_{ijkl} = \frac{1}{4\sigma_{\text{crit}}^2}\left(A_{ik}A_{jl} + A_{il}A_{jk}\right),$$

(83)

where σ_{crit} denotes the reference critical stress associated with uniaxial loading in a certain axis that can be conceptually replaced by an ultimate stress. The second-order anisotropy tensor $(\mathbf{A})_{ij}$ in (83), expressed in index notation for $i, j, k, l \in \{1, 2, 3\}$, deals with the mechanical response of orthotropic, transversely isotropic and isotropic materials. Details concerning how to construct the tensor **A** can be found in Raina and Miehe [46]. For a simplified case, when the principal axes coincide with the axes of reference, the crack driving force in (82) turns into

$$\overline{\mathscr{H}} = \sum_{i=1}^{3}\left(\frac{\left\langle \sigma_{0_i}\right\rangle}{\sigma_{\text{crit}}/\mathfrak{a}_i}\right)^2 .$$

(84)

It needs to be emphasized that $\mathfrak{a}_i$ are scaling factors to impose a certain class of material, e.g., transversely isotropic material, which also enters in $(\mathbf{A})_{ij}$.

4. Decoupled weak formulation

This section is devoted to a Galerkin-type weak formulation of the strong forms presented in Section 2. In particular, a staggered solution procedure is implemented, where the coupled Euler–Lagrange equations are successively solved on the basis of a one-pass operator-splitting algorithm on the temporal side, whereas a Galerkin-type weak formulation on the spatial side furnishes the rate-dependent formulation of the phase-field. Such a solution algorithm sequentially updates the crack phase-field and the deformation map in a typical time step by means of a Newton–Raphson scheme.

4.1. One-pass operator-splitting algorithm

We first perform a decoupling of the mechanical and crack phase-field sub-problems by the virtue of a one-pass operator-splitting algorithm composed of two sub-algorithms, i.e.

$$\mathrm{ALGO}_{\mathrm{CM}} = \mathrm{ALGO}_{\mathrm{C}} \circ \mathrm{ALGO}_{\mathrm{M}},$$

(85)

for a typical time increment $\boldsymbol{\tau} = t_{n+1} - t_n$, where t_{n+1} and t_n stand for the current and previous time steps, respectively. For the sake of keeping the notation compact, all field variables without subscript are hereinafter evaluated at time t_{n+1}. The operator-splitting algorithm basically converts the non-convex coupled problem into two convex and symmetric sub-problems which are computationally more feasible than the monolithic scheme. The algorithm of each subproblem reads

$$\text{(M)}: \begin{cases} J\mathrm{div}\left(J^{-1}\boldsymbol{\tau}\right) + \rho_0 \tilde{\boldsymbol{\gamma}} = \mathbf{0}, \\ \dot{d} = 0, \end{cases} \quad \text{(C)}: \begin{cases} \dot{\boldsymbol{\varphi}} = \mathbf{0}, \\ d - \nabla d \cdot \mathscr{L} \nabla d - 2(1-d)\mathscr{H} + \eta \dot{d} = 0. \end{cases}$$

(86)

The algorithm (M) is the mechanical predictor step which is solved for the frozen crack phase-field parameter $d = d_n$, while the algorithm (C) is the crack evolution step for the frozen deformation map $\boldsymbol{\varphi} = \boldsymbol{\varphi}_n$.

4.2. Time-discrete weak formulation

We construct the weak forms of the balance of linear momentum $(53)_1$ and the rate-dependent evolution equation of the crack phase-field (60). For the quasi-static problem under consideration, we introduce two test function fields $\delta\boldsymbol{\varphi}$ and δd, regarded as the virtual deformation and the crack phase-field, respectively. Thereby, $\delta\boldsymbol{\varphi}$ and δd satisfy the homogeneous form of the Dirichlet boundary conditions on their corresponding reference surfaces $\partial\mathscr{B}_{\varphi}$ and $\partial\mathscr{B}_{d}$ according to

$$\delta\boldsymbol{\varphi} \in \mathscr{W}_{\delta\varphi} = \left\{ \delta\boldsymbol{\varphi} \,\middle|\, \delta\boldsymbol{\varphi} = \mathbf{0} \quad \text{on} \quad \partial\mathscr{B}_{\varphi} \right\}, \quad \delta d \in \mathscr{W}_{\delta d} = \left\{ \delta d \,\middle|\, \delta d = 0 \quad \text{on} \quad \partial\mathscr{B}_{d} \right\}.$$

(87)

A conventional Galerkin procedure leads to the weighted residual expressions of the field variables for the mechanical problem, i.e.

$$G^{\varphi} = G^{\varphi}_{\text{int}}(\delta\boldsymbol{\varphi}, \boldsymbol{\varphi}, d) - G^{\varphi}_{\text{ext}}(\delta\boldsymbol{\varphi}) = 0,$$

(88)

and the phase-field problem

$$G^{d} = G^{d}_{\text{int}}(\delta d, \boldsymbol{\varphi}, d) - G^{d}_{\text{ext}}(\delta d) = 0.$$

(89)

The term G^{φ}_{ext} in (88) represents the external weighted-residual due to the action of $\tilde{\boldsymbol{\gamma}}$ and $\tilde{\mathbf{t}}$, whereas the term for the phase-field in (89) vanishes $\left(G^{d}_{\text{ext}} = 0\right)$, see Gültekin et al. [10]. The explicit expressions for G^{φ}_{int} and G^{d}_{int} with respect to (86) read

$$\begin{aligned} G^{\varphi}_{\text{int}} &= \int_{\mathscr{B}} \mathbf{g}\, \nabla_x(\delta\boldsymbol{\varphi}) : \boldsymbol{\tau}\, \mathrm{d}V, \\ G^{d}_{\text{int}} &= \int_{\mathscr{B}} \left\{ \delta d \left[d - 2(1-d)\mathscr{H} + \eta \frac{d - d_n}{\tau} \right] + \nabla(\delta d) \cdot \mathscr{L}\, \nabla d \right\} \mathrm{d}V\,. \end{aligned}$$

(90)

A reliable and efficient solution of the above-mentioned equations entails a consistent linearization with respect to all quantities, i.e. $\boldsymbol{\varphi}$ and d, associated with the nonlinear problem about $\boldsymbol{\varphi} = \tilde{\boldsymbol{\varphi}}$ and $d = \tilde{d}$. Thus,

$$\begin{aligned} \mathrm{Lin} G^{\varphi}\big|_{\tilde{\boldsymbol{\varphi}}} &= G^{\varphi}(\delta\boldsymbol{\varphi}, \tilde{\boldsymbol{\varphi}}, d) + \Delta G^{\varphi}(\delta\boldsymbol{\varphi}, \tilde{\boldsymbol{\varphi}}, d; \Delta\boldsymbol{\varphi}) = 0, \\ \mathrm{Lin} G^{d}\big|_{\tilde{d}} &= G^{d}(\delta d, \boldsymbol{\varphi}, \tilde{d}) + \Delta G^{d}(\delta d, \boldsymbol{\varphi}, \tilde{d}; \Delta d) = 0. \end{aligned}$$

(91)

The expressions in (91) are given by the Taylor's expansion through the Gâteaux derivative yielding the linear incremental terms ΔG^{φ} and ΔG^{d}, which are decomposed in the following way

$$\Delta G^{\varphi} = \Delta G^{\varphi}_{\text{int}} - \Delta G^{\varphi}_{\text{ext}}, \quad \Delta G^{d} = \Delta G^{d}_{\text{int}} - \Delta G^{d}_{\text{ext}}.$$

(92)

While the external terms vanish (Gültekin et al. [10]), the explicit forms of the internal terms are given as

$$\begin{aligned}\Delta G^{\varphi}_{\text{int}} &= \int_{\mathscr{B}} \mathbf{g}\nabla_x(\delta\boldsymbol{\varphi}) : \mathbb{C} : \mathbf{g}\nabla_x(\Delta\boldsymbol{\varphi})\mathrm{d}V + \int_{\mathscr{B}} \nabla_x(\delta\boldsymbol{\varphi}) : \nabla_x(\Delta\boldsymbol{\varphi})\boldsymbol{\tau}\mathrm{d}V \\ \Delta G^{d}_{\text{int}} &= \int_{\mathscr{B}} \delta d\left(1 + 2\mathscr{H} + \frac{\eta}{\tau}\right)\Delta d\mathrm{d}V + \int_{\mathscr{B}} \nabla(\delta d)\cdot\mathscr{L}\nabla(\Delta d)\mathrm{d}V,\end{aligned}$$

(93)

where the Eulerian elasticity tensor $\mathbb{C}$ takes on the form $\mathbb{C} = g(d)\left(\mathbb{C}_0^{\text{iso}} + \mathbb{C}_0^{\text{ani}}\right)$.. The spatial discretization of the time-discrete decoupled weak forms in (90) and their corresponding linearizations documented in (93), provide their algebraic counterparts, namely the discrete residual vectors and the stiffness matrices. For an elaborate treatment of discretization methods and a staggered solution procedure based on a one-pass operator-splitting algorithm we refer to, e.g., Miehe et al. [33] and Gültekin et al. [10]. A general outlook of the staggered solution scheme is provided in Table 1.

5. Representative numerical examples

We start by demonstrating the effect of the anisotropic crack phase-field model on the propagation of the crack, in particular a sensitivity analysis is provided. Subsequently, the anisotropic failure criteria imparted in Section 3 are scrutinized from a numerical point of view, i.e. the failure surface and the crack propagation associated with the distinct failure criteria are compared with each other on the basis of simple numerical examples.

5.1. Sensitivity analysis of the anisotropic phase-field model

In order to show the purely geometric effect that the anisotropy tensor $\mathscr{L}$ grants to the phase-field formulation, a 2-D square benchmark problem, as described in Fig. 6(a) and (b), is considered. This problem, unlike the majority of the examples in the crack phase-field literature, is performed in the absence of the mechanical field. The benchmark displays an anisotropic propensity via a single family of fibers **M**, oriented by an angle of $\alpha = 30°$ with respect to the x-axis. The (unstructured) finite element mesh consists of 10 362 four-noded quadrilateral elements. The phase-field parameter d is assigned a unit value within a disc with 1 mm in diameter at the center of the domain thereby creating a difference between the surfaces energies ($g_c\Gamma(d)$) of the disc and the rest of the domain. The computations performed for the evolution of the crack phase-field (ALGO_{C}) in a typical Newton iteration

yield the diffusion of the phase-field for different values of the anisotropy parameter $\omega_{\mathrm{M}} = \{0, 1, 5, 10\}$, see Fig. 6(c)–(f), respectively. In fact, the evolution of the phase-field parameter d starts to diverge from being isotropic (Fig. 6(c)), and becomes oriented along the direction of the fibers as the anisotropy parameter ω_{M} increases (Fig. 6(d)–(f)). This palpably suggests that the proposed model can handle transitions from isotropic to weak and strong anisotropy.

5.2. Numerical investigation of the failure surfaces

This investigation deals with a homogeneous problem of a unit cube discretized by one hexahedral element (Fig. 7(a)) that resolves the analytical solution for the deformation and the stress fields as all non-local effects due to the gradient of the crack phase-field ∇d are discarded. The effect of the length-scale parameter vanishes since I approaches to unity. As a loading protocol, we first consider separate uniaxial extension tests along the x-, y- and z-directions with a stretch ratio $\lambda_x = \lambda_y = \lambda_z \equiv 2$ which is followed by a series of planar biaxial deformations in the xy-plane with stretch ratios $\lambda_x : \lambda_y = 2 : 1.1, 2 : 1.25, 2 : 1.5, 2 : 1.75, 2 : 2, 1.75 : 2, 1.5 : 2, 1.25 : 2, 1.1 : 2$. Stretch ratios in the xz- and yz-planes $\lambda_x : \lambda_z$ and $\lambda_y : \lambda_z$ are applied in an analogous manner as for $\lambda_x : \lambda_y$, see Fig. 7(b)–(d). The tissue is regarded as transversely isotropic consisting of one family of fibers with orientation $\mathbf{M}$ along the x-direction, and it is embedded in the ground matrix. The elastic material parameters and the crack phase-field parameters are listed for each failure criterion in Table 2.

Fig. 8(a)–(c) illustrates the resulting failure surfaces at the instance when $d \neq 0$ for the energy-based criterion, the Tsai–Wu criterion and the principal stress criterion, respectively. The results of simulations conspicuously manifest the transverse isotropy of the three failure criteria as the failure surfaces are elliptical in shape (only one eight of an ellipsoid is shown due to the tensile characteristic of the deformation). The onset of crack occurs when the normal stress $\sigma_{xx} \approx 140$kPa, whilst the value of the other normal stresses σ_{yy} and σ_{zz} are around 20kPa. It needs to be emphasized that one can envisage a zone between the macroscopic onset ($d \neq 0$) and the completion ($d = 1$) of the crack in the context of diffusive crack modeling such as the crack phase-field. This example points out the associated macroscopic onset of the crack.

Fig. 8(d) demonstrates the failure surfaces obtained at $d \neq 0$ for the Hill criterion. We note that the Hill criterion becomes in line with the von Mises–Huber criterion for the isotropic situation, namely the yz-plane. With the specified deformations the criterion cannot be satisfied when $\sigma_x^{\mathrm{u}} = 140$ kPa and $\sigma_y^{\mathrm{u}} = \sigma_z^{\mathrm{u}} = 20$ kPa. In fact, the failure envelope on the isotropic yz-plane becomes open-ended. Therefore, a different set of phase-field parameters are used, as listed in Table 2 in order to retrieve a closed-ended failure surface. The distinct shape of the failure envelope on the yz-plane eventually becomes discernable, see Fig. 8(d), which retrieves the von Mises–Huber criterion, as expected.

5.3. Uniaxial extension test investigated with different failure criteria

This benchmark represents a notched strip of a hypothetical arterial tissue with two families of fibers oriented in the directions $\mathbf{M}$ and $\mathbf{M}'$ and symmetrically arranged with respect to

the x-axis by an angle α. The fibers correspond to the collagenous component of the tissue. The geometric setup and the loading condition are indicated in Fig. 9(a). The finite element mesh consists of 35 163 four-node tetrahedral elements connected by 7 553 nodes, and it comprises a refined zone beyond the notch where the crack is expected to propagate, see Fig. 9(b). As stated by Miehe et al. [33], in order to resolve the crack zone properly, the length-scale parameter l needs to be chosen at least twice as large as the minimum mesh size realized in the refined region. Accordingly, the length-scale parameter is selected as $l = 0.06$ mm, and the viscosity η is set to zero. The weak anisotropy as corroborated by experimental results (see, e.g., Fig. 1 in [10]) is accommodated by the anisotropy parameters $\omega_{\mathrm{M}} = \omega_{\mathrm{M}}{}' = 1.0$. The displacements are constrained in the planes $x = 0$, $y = 0$, and $z = 0$ along the x-, y-, and z-directions, respectively. The used elastic material parameters and the crack phase-field parameters are summarized in Table 3.

The crack growth with respect to each failure criterion is analyzed for a monotonic load pattern driven by the displacement u throughout the numerical simulation, whereby the performance of the failure criteria is assessed in terms of their ability to mimic the crack propagation resulting in a complete rupture of the strip. Table 4 summarizes the number of simulation steps times step sizes considered for each criterion.

Fig. 10 depicts the evolution of the crack phase-field d with respect to the four failure criteria at instants t_1, t_2, t_3 and t_4. The crack in the first and last case, namely the energy-based and the Hill criterion (Fig. 10(a) and (d)), grows by following a nearly straight pattern in the refined zone upon its initiation at the tip of the notch. However, both the Tsai–Wu and the principal stress criteria (Fig. 10(b) and (c)) show a spurious crack branching, not observed experimentally, see, e.g., Fig. 1 in [10]. The damaged zone also spreads out of the refined region. In this respect, the Hill criterion provides a more physically admissible picture than the other stress-based criteria albeit the crack front still remains spurious compared with that of the energy-based one. In fact, the energy-based criterion predicts a smoother crack-front than all stress-based criteria.

Fig. 11 illustrates curves that correspond to force F vs displacement u and to crack driving force $\overline{\mathscr{H}}$ vs time t, where the particular instants t_1, t_2, t_3 and t_4 are indicated for each failure criterion. As can be seen, a typical nonlinear response is followed by a sudden decrease in the load-bearing capacity, while a dramatic increase in the value of the crack driving force becomes evident upon the onset of macro-cracks at the tip of the notched region. Note that the force–displacement curves are obtained at the plane $x = 12$ mm, whereas the crack driving force–time curves are depicted for a node just beyond the tip of the notch. The isotropic and anisotropic contributions due to $\overline{\mathscr{H}}^{\mathrm{iso}}$ and $\overline{\mathscr{H}}^{\mathrm{ani}}$ are discernable for the energy-based failure criterion. What is also intriguing is that there exists at least two orders of magnitude difference between the energy-based and the stress-based criteria in terms of the values of the crack driving forces. That entails the use of smaller step sizes for all stress-based criteria after the fully initiated crack (indicated in Table 4) to avoid an unstable crack growth which may eventually lead to the loss of global convergence, and a sudden crush of the simulation.

5.4. Peel test investigated with different failure criteria

Peel tests bear an immense resemblance to the physical phenomena of, e.g., aortic dissections and allow a computational analysis of the dissection propagation in terms of various failure criteria mentioned in Section 3. The benchmark involves an initial tear at the middle, and idealizes an arterial wall with a morphology rendered by a single family of fibers **M** oriented in the y-direction, see Fig. 12(a). We imitate the tailored geometry provided by Gasser and Holzapfel [25] and discretize the strip with 2 640 eight-node hexahedral elements connected by 5 536 nodes, see Fig. 12(b). Appropriate Dirichlet and Neumann-type boundary conditions are considered in order to avoid rigid body motions. A horizontal displacement $u_x = 4$ mm is incrementally applied at the arms on the top plane in the x-direction, while all nodes on the plane at $y = 0$ are fixed in all directions, see Fig. 12(a). In addition, the displacements in the z-direction are prevented to reflect the plain strain condition.

As to the elastic material parameters, we adopt $\mu = 16.2$kPa, $k_1 = 98.1$kPa and $k_2 = 10$ according to Gasser and Holzapfel [25]. The penalty parameter and the length-scale parameter are chosen as $\kappa = 1000$kPa and $l = 0.05$ mm, respectively. The viscosity parameter is adjusted to be $\eta = 1$kPa s for the energy-based criterion and $\eta = 10$kPa s for the stress-based criteria, while the anisotropy parameters are selected as $\omega_{\mathrm{M}} = 1.0$ and $\omega_{\mathrm{M}}' = 0$. The other phase-field parameters are taken from Table 5.

Fig. 13 depicts the spatial distribution and the evolution of the crack phase-field for the energy-based, Tsai–Wu, principal stress and the Hill criterion, as the two arms of the strip separated by an initial tear are being pulled in opposite directions. The problems associated with all stress-based criteria in the previous example, see Section 5.3, seem to resume and they can only be circumvented via the use of smaller step sizes, see Table 6. Besides, the phasefield also evolves at locations where two arms bend which is also demonstrated by Ferrara and Pandolfi [20] as regions of higher stress concentrations compared with the dissecting zone at the middle. This undesired behavior is not present in the case of the energy-based criterion.

In Fig. 14 the force per unit width is plotted against the displacement applied (the separation of one arm) in regard to the energy-based, Tsai–Wu, principal stress and the Hill criterion. A weakly nonlinear response is observed until the ultimate load bearing capacity is reached, which is realized by a kind of plateau region. The load bearing capacity significantly diminishes afterwards for all failure criteria. It needs to be highlighted that the computation suffers due to incomplete convergence discernable from the jags in the loading path for the stress-based criteria, see Fig. 14(b)–(d).

6. Discussion

The most likely cause of numerical instability related with stress-based criteria may be that these criteria are essentially driven by the effective complementary energy $\Psi_{0_{\mathrm{com}}}$ through the fourth-order strength tensor which is the analogue of the elastic compliance tensor. However, energy-based criteria are governed by the effective strain energy $\Psi_{0_{\mathrm{Str}}}$ *per se*. As a

result, the changes $\Delta\Psi_{0_{\text{com}}}$ and $\Delta\Psi_{0\text{str}}$ are not equivalent in a typical time increment $\Delta t = t_{n+1} - t_n$ provided that the mechanical response of the material is nonlinear – typically the stress in a tissue grow faster at finite strains. Note that the two terms are interchangeable for the case of linear elasticity or in the context of small strains. In conclusion, the typical exponential nature of the stress–stretch relationship in soft biological tissues renders stressbased criteria non-functional. Fig. 15 illustrates a qualitative sketch elucidating how the equivalence between $\Delta\Psi_{0_{\text{com}}}$ and $\Delta\Psi_{0\text{str}}$ changes in the favor of $\Delta\Psi_{0_{\text{com}}}$ as the response of the material becomes highly nonlinear which utterly leads to an unstable crack growth. This phenomenon presents itself conspicuously in magnitudes of the dimensionless crack driving forces in Fig. 11 of Section 5.3.

The multi-field variational formulation leads to Euler–Lagrange equations governing the crack phase-field evolution and the static equilibrium in the absence of inertial effects. Hence, the derived formulation inherently leads to the crack path which minimizes the energy and maximizes the dissipation through the crack propagation process. However, the stress-based failure criteria merely describe the elastic domain of a brittle anisotropic material corresponding to the onset of the macro-cracks. The magnitudes of stress-based criteria beyond the failure surface do not necessarily lead to maximum dissipation or a minimum energy state since they can only be incorporated into the crack phase-field evolution equation on a rather *ad hoc* basis by taking the advantage of the crack driving force being dimensionless. As a matter of fact, the variational formulation does not hold for stress-based criteria producing a cracked zone in certain directions which may not correspond to a maximum dissipation or a minimum energy state of the effective material. Therefore, as evidently noticed in Sections 5.3 and 5.4, stress-based criteria are not able to portray physically relevant post-cracking states. However, in biomechanical applications, e.g., rupture of thoracic aortas, where not only the crack initiation but also the crack propagation is of fundamental concern, an energy criterion prevails.

The plots in Fig. 14 showing the force per unit width against the applied displacement seem to fall short of reproducing an asymptotic jagged plateau unlike those of Gasser and Holzapfel [25] and Ferrara and Pandolfi [20]. Nevertheless, the sensitivity analyses of [20] in the sense of mesh size and strength values suggest similar postcracking states as in Fig. 14 when the analysis is performed by using a relatively coarse mesh along with high strength values. However, our study primarily spotlights the comparison of numerical performances obtained for various failure criteria. At this stage we do not look for model parameters that are fitted to experimental data.

7. Conclusion

In the present study we have compared a number of anisotropic failure criteria, essentially based on the free energy or the stress, with respect to their ability to capture admissible anisotropic failure surfaces and crack propagations for simple boundary-value problems. On the theoretical side, the crack phase-field model, established according to a continuous variational setup due to a power balance, provided the backbone of our modeling endeavors. In the sequel, this framework was extended to the local rate-dependency of the phase-field

evolution. The resulting Euler–Lagrange equations were recast by simple algebraic manipulations, and then solved by a one-pass operator-splitting algorithm on the temporal side which was ensued by a Galerkin-type weak formulation on the spatial side. On the constitutive part, a short summary of the energy-based criterion was given from our previous contribution. Subsequently, we introduced stress-based criteria (Tsai–Wu and Hill) together with the principal stress criterion.

On the numerical side, we focused on the anisotropic evolution of the crack phase-field. This was followed by the comparison of failure surfaces associated with the aforementioned criteria dealing with a homogeneous problem. The second investigation was performed on a notched strip of a hypothetical arterial tissue undergoing uniaxial extension, whereby the corresponding crack growth for each failure criterion was demonstrated. Finally, peel tests of a hypothetical arterial strip subjected to the aforementioned failure criteria were performed, and the respective dissections were systematically examined. The results of the simulations in Section 5.2 suggest that the energy-based criterion and the stress-based criteria, namely the Tsai–Wu and the principal stress criterion, can reflect the onset of the crack where the expected failure surfaces attributed to the transverse isotropy were acquired; however, the tests on the propagation of the crack in Sections 5.3 and 5.4 evidently favor the energetic-based criterion to accomplish a stable crack growth for the analyzed three-dimensional boundary-value problems blended with anisotropy at finite strains.

Acknowledgments

H.D. gratefully acknowledges financial support from TUBITAK (BIDEB 2232, Project # 114C073), while O.G. acknowledges financial support from the National Institutes of Health (research grant no. NIH 7R01HL117063–03).

References

[1]. Humphrey JD, Holzapfel GA, Mechanics, mechanobiology, and modeling of human abdominal aorta and aneurysms, J. Biomech 45 (2012) 805–814. [PubMed: 22189249]

[2]. Kim JH, Avril S, Duprey A, Favre JP, Experimental characterization of rupture in human aortic aneurysms using a full-field measurement technique, Biomech. Model. Mechanobiol 11 (2012) 841–853. [PubMed: 22048330]

[3]. Chatzizisis YS, Coşkun AÜ, Jonas M, Edelman ER, Feldman CL, Stone PH, Role of endothelial shear stress in the natural history of coronary atherosclerosis and vascular remodeling: molecular, cellular, and vascular behavior, J. Am. Coll. Cardiol 49 (2007) 2379–2393. [PubMed: 17599600]

[4]. Holzapfel GA, Sommer G, Regitnig P, Anisotropic mechanical properties of tissue components in human atherosclerotic plaques, J. Biomech. Eng 126 (2004) 657–665. [PubMed: 15648819]

[5]. Criado FJ, Aortic dissection: a 250-year perspective, Tex. Heart Inst. J 38 (2011) 694–700. [PubMed: 22199439]

[6]. Roccabianca S, Ateshian GA, Humphrey JD, Biomechanical roles of medial pooling of glycosaminoglycans in thoracic aortic dissection, Biomech. Model. Mechanobiol 13 (2014) 13–25. [PubMed: 23494585]

[7]. Lee JK, Yao L, Phelps CT, Wirth CR, Czajka J, Lozman J, Anterior cruciate ligament tears: MR imaging compared with arthroscopy and clinical tests, Radiology 166 (1988) 861–864. [PubMed: 3340785]

[8]. Weiss JA, Gardiner JC, Computational modeling of ligament mechanics, Crit. Rev. Biomed. Eng 29 (2001) 303–371. [PubMed: 11730098]

[9]. Sharma P, Maffulli N, Tendon injury and tendinopathy: healing and repair, J. Bone Joint Surg. 87 (2005) 187–202. [PubMed: 15634833]

[10]. Gültekin O, Dal H, Holzapfel GA, A phase-field approach to model fracture of arterial walls: theory and finite element analysis, Comput. Methods Appl. Mech. Engrg 312 (2016) 542–566.

[11]. Tsai SW, Hahn HT, Introduction to Composite Materials, Technomic Publishing Company, Lancaster, 1980.

[12]. Talreja R, Singh CV, Damage and Failure of Composite Materials, Cambridge University Press, Cambridge, 2012.

[13]. Hill R, A theory of the yielding and plastic flow of anisotropic metals, Proc. R. Soc. Lond. Ser. A 193 (1948) 281–297.

[14]. Azzi VD, Tsai SW, Anisotropic strength of composites, Exp. Mech 5 (1965) 283–288.

[15]. Tsai SW, Wu EM, A general theory of strength of anisotropic materials, J. Compos. Mater 5 (1971) 58–80.

[16]. Hashin Z, Failure criteria for unidirectional fiber composites, J. Appl. Mech 47 (1980) 329–334.

[17]. Wolfe WE, Butalia TS, A strain–energy based failure criterion for non-linear analysis of composite laminates subjected to biaxial loading, Compos. Sci. Technol 58 (1998) 1107–1124.

[18]. Ortiz M, Pandolfi A, Finite-deformation irreversible cohesive elements for three-dimensional crack-propagation analysis, Int. J. Numer. Meth. Engng 44 (1999) 1267–1282.

[19]. Ferrara A, Pandolfi A, Numerical modeling of fracture in human arteries, Comput. Methods Biomech. Biomed. Eng 11 (2008) 553–567.

[20]. Ferrara A, Pandolfi A, A numerical study of arterial media dissection processes, Int. J. Fracture 166 (2010) 21–33.

[21]. Simo JC, Oliver J, Amero F, An analysis of strong discontinuities induced by strain softening in rate-independent inelastic solids, Comput. Mech 12 (1993) 277–296.

[22]. Linder C, Armero F, Finite elements with embedded branching, Finite Elem. Anal. Des 45 (2009) 280–293.

[23]. Belytschko T, Black T, Elastic crack growth in finite elements with minimal remeshing, Int. J. Numer. Meth. Engng 45 (1999) 601–620.

[24]. Moës N, Dolbow J, Belytschko T, A finite element method for crack growth without remeshing, Int. J. Numer. Meth. Engng 46 (1999) 131–150.

[25]. Gasser TC, Holzapfel GA, Modeling the propagation of arterial dissection, Eur. J. Mech. A Solids 25 (2006) 617–633.

[26]. Dal H, Kaliske M, A micro-continuum-mechanical material model for failure of rubber-like materials: Application to aging-induced fracturing, J. Mech. Phys. Solids 57 (2009) 1340–1356.

[27]. Griffith AA, The phenomena of rupture and flow in solids, Philos. Trans. R. Soc. Lond. A 221 (1921) 163–197.

[28]. Irwin GR, Fracture mechanics, in: Goodier JN, Hoff NJ (Eds.), Structural Mechanics, Pergamon Press, New York, 1960, pp. 557–594.

[29]. Francfort GA, Marigo J-J, Revisiting brittle fracture as an energy minimization problem, J. Mech. Phys. Solids 46 (1998) 1319–1342.

[30]. Bourdin B, Francfort GA, Marigo J-J, Numerical experiments in revisited brittle fracture, J. Mech. Phys. Solids 48 (2000) 797–826.

[31]. Mumford D, Shah J, Optimal approximations by piecewise smooth functions and associated variational problems, Comm. Pure Appl. Math 42 (1989) 577–685.

[32]. Amborosio L, Tortorelli VM, Approximation of functionals depending on jumps by elliptic functionals via γ-convergence, Comm. Pure Appl. Math 43 (1990) 999–1036.

[33]. Miehe C, Welschinger F, Hofacker M, Thermodynamically consistent phase-field models of fracture: Variational principles and multi-field FE implementations, Int. J. Numer. Meth. Engng 83 (2010) 1273–1311.

[34]. Miehe C, Hofacker M, Welschinger F, A phase field model for rate-independent crack propagation: robust algorithmic implementation based on operator splits, Comput. Methods Appl. Mech. Engrg 199 (2010) 2765–2778.

[35]. Borden MJ, Verhoosel CV, Scott MA, Hughes TJR, Landis CM, A phase-field description of dynamic brittle fracture, Comput. Methods Appl. Mech. Engrg 217–220 (2012) 77–95.

[36]. Hofacker M, Miehe C, A phase-field model of dynamic fracture: robust field updates for the analysis of complex crack patterns, Int. J. Numer. Meth. Engng 93 (2013) 276–301.

[37]. Miehe C, Schänzel L-M, Ulmer H, Phase field modeling of fracture in multi-physics problems. Part I. Balance of crack surface and failure criteria for brittle crack propagation in thermo-elastic solids, Comput. Methods Appl. Mech. Engrg 294 (2015) 449–485.

[38]. Miehe C, Hofacker M, Schänzel L-M, Aldakheel F, Phase field modeling of fracture in multi-physics problems. Part II. Coupled brittle-to-ductile failure criteria and crack propagation in thermo-elastic–plastic solids, Comput. Methods Appl. Mech. Engrg 294 (2015) 486–522.

[39]. Miehe C, Dal H, Schänzel L-M, Raina A, A phase-field model for chemo-mechanical induced fracture in lithium-ion battery electrode particles, Int. J. Numer. Meth. Engng 106 (2016) 683–711.

[40]. Cahn JW, Hilliard JE, Free energy of a nonuniform system. I. Interfacial free energy, J. Chem. Phys 28 (1958) 258–267.

[41]. Li B, Peco C, Millan D, Arias I, Arroyo M, Phase-field modeling and simulation of fracture in brittle materials with strongly anisotropic surface energy, Int. J. Numer. Meth. Engng 102 (2015) 711–727.

[42]. Teichtmeister S, Kienle D, Aldakheel F, Keip M-A, Phase-field modeling of fracture in anisotropic brittle solids, Int. J. Non-Linear Mech. 97 (2017) 1–21.

[43]. Clayton JD, Kanp J, Phase field modeling of directional fracture in anisotropic polycrystals, Comput. Mater. Sci 98 (2015) 158–169.

[44]. Nguyen T-T, Réthéro J, Yvonnet J, Baietto M-C, Multi-phase-field modeling of anisotropic crack propagation for polycrystalline materials, Comput. Mech 60 (2017) 289–314.

[45]. Gültekin O, A Phase Field Approach to the Fracture of Anisotropic Medium, University of Stuttgart, Institute of Applied Mechanics (CE), Pfaffenwaldring 7, Stuttgart, 2014 Master'S Thesis.

[46]. Raina A, Miehe C, A phase-field model for fracture in biological tissues, Biomech. Model. Mechanobiol 15 (2016) 479–496. [PubMed: 26165516]

[47]. Perzyna P, Thermodynamic theory of viscoplasticity, Adv. Appl. Mech 9 (1966) 243–377.

[48]. Eringen AC, Nonlinear Theory of Continuous Media, McGraw-Hill Book Company, Inc., New York, 1962.

[49]. Truesdell C, Noll W, in: Flügge S (Ed.), The Non-Linear Field Theories of Mechanics, in: Encyclopedia of Physics, vol. III, Springer-Verlag, Berlin, 1965.

[50]. Spencer AJM, Part III Theory of invariants, in: Eringen AC (Ed.), Continuum Physics, Volume I – Mathematics, Academic Press, New York, 1971, pp. 239–353.

[51]. Marsden JE, Hughes TJR, Mathematical Foundations of Elasticity, Dover, New York, 1994.

[52]. Miehe C, Numerical computation of algorithmic (consistent) tangent moduli in large-strain computational inelasticity, Comput. Methods Appl. Mech. Engrg 134 (1996) 223–240.

[53]. Holzapfel GA, Nonlinear Solid Mechanics. A Continuum Approach for Engineering, John Wiley & Sons, Chichester, 2000.

[54]. Gurtin ME, Fried E, Anand L, The Mechanics and Thermodynamics of Continua, Cambridge University Press, New York, 2010.

[55]. Borden MJ, Hughes TJR, Landis CM, Verhoosel CV, A higher-order phase-field model for brittle fracture: Formulation and analysis within the isogeometric analysis framework, Comput. Methods Appl. Mech. Engrg 273 (2014) 100–118.

[56]. Holzapfel GA, Gasser TC, Ogden RW, A new constitutive framework for arterial wall mechanics and a comparative study of material models, J. Elasticity 61 (2000) 1–48.

[57]. Borden MJ, Hughes TJR, Landis CM, Anvari A, Lee IJ, A phase-field formulation for fracture in ductile materials: Finite deformation balance law derivation, plastic degradation, and stress triaxiality effects, Comput. Methods Appl. Mech. Engrg 312 (2016) 130–166.

[58]. Bourdin B, Francfort GA, Marigo J-J, The Variational Approach to Fracture, Springer-Verlag, Berlin, 2008.

[59]. Kachanov LM, Time of the rupture process under creep conditions, Izvestija Akademii Nauk Sojuza Sovetskich Socialisticeskich Respubliki (SSSR) Otdelenie Techniceskich Nauk (Moskra) 8 (1958) 26–31.

[60]. Miehe C, A multi-field incremental variational framework for gradient-extended standard dissipative solids, J. Mech. Phys. Solids 59 (2011) 898–923.

[61]. Miehe C, Schänzel L-M, Phase field modeling of fracture in rubbery polymers. Part I. Finite elasticity coupled with brittle fracture, J. Mech. Phys. Solids 65 (2014) 93–113.

[62]. Miehe C, Discontinuous and continuous damage evolution in ogden-type large-strain elastic materials, Eur. J. Mech. A Solids 14 (1995) 697–720.

[63]. Simo JC, Hughes TJR, Computational Inelasticity, Springer-Verlag, New York, 1998.

[64]. Pipes RB, Cole BW, On the off-axis strength test for anisotropic material 1, J. Compos. Mater 7 (1973) 246–256.

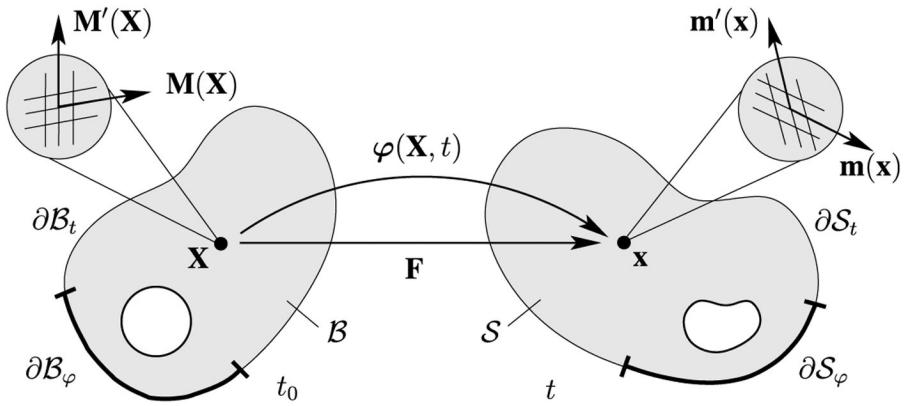

Fig. 1.

Nonlinear deformation of an anisotropic solid with the reference configuration $\mathscr{B} \in \mathbb{R}^3$ and the spatial configuration $\mathscr{S} \in \mathbb{R}^3$. nonlinear deformation map is $\boldsymbol{\varphi}: \mathscr{B} \times \mathscr{T} \rightarrow \mathscr{S}$, which transforms a material point $\mathbf{X} \in \mathscr{B}$ onto a spatial point $\mathbf{x} = \boldsymbol{\varphi}(\mathbf{X}, t) \in \mathscr{S}$ at time t. The anisotropic micro-structure material point $\mathbf{X}$ is rendered by two families of fibers with unit vectors $\mathbf{M}$ and $\mathbf{M}'$. Likewise, the anisotropic micro-structure of the spatial point $\mathbf{x}$ is described by $\mathbf{m}$ and $\mathbf{m}'$, as the spatial counterparts of $\mathbf{M}$ and $\mathbf{M}'$, respectively.

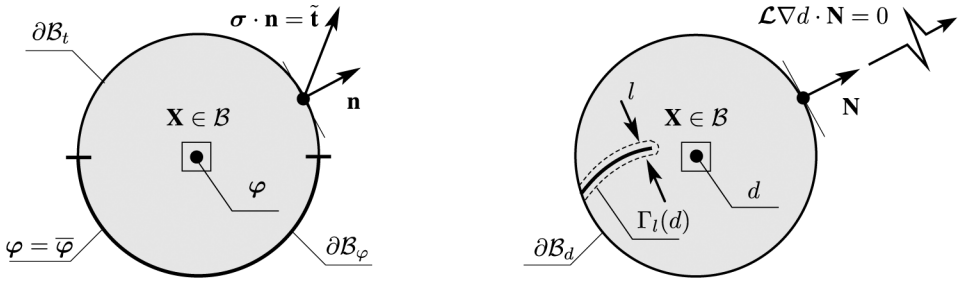

(a) Deformation field. (b) Crack phase-field.

Fig. 2.

Multi-field problem: (a) mechanical problem of deformation along with Dirichlet and Neumann-type boundary conditions actualized by $\boldsymbol{\varphi}=\overline{\boldsymbol{\varphi}}$ and the Cauchy theorem $\boldsymbol{\sigma}\cdot\mathbf{n}=\tilde{\mathbf{t}}$, respectively; (b) evolution of the crack phase-field problem with the Neumann-type boundary condition $\mathscr{L}\nabla d\cdot\mathbf{N}=0$.

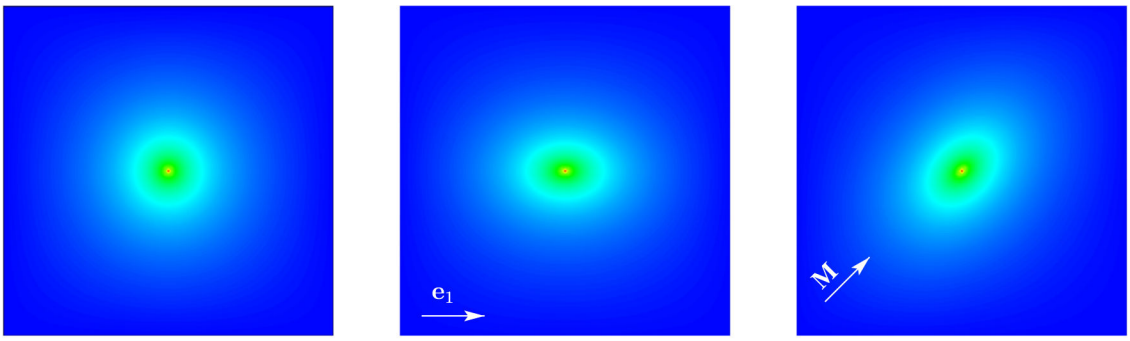

(a) $\boldsymbol{\mathcal{L}} = l^2\mathbf{I}$. (b) $\boldsymbol{\mathcal{L}} = l^2(\mathbf{I} + \mathbf{e}_1 \otimes \mathbf{e}_1)$. (c) $\boldsymbol{\mathcal{L}} = l^2(\mathbf{I} + \mathbf{M} \otimes \mathbf{M})$.

Fig. 3.

(a) Isotropic damage field; (b) anisotropic damage field with fiber angle $\alpha = 0°$; (c) anisotropic damage field with $\alpha = 45°$.

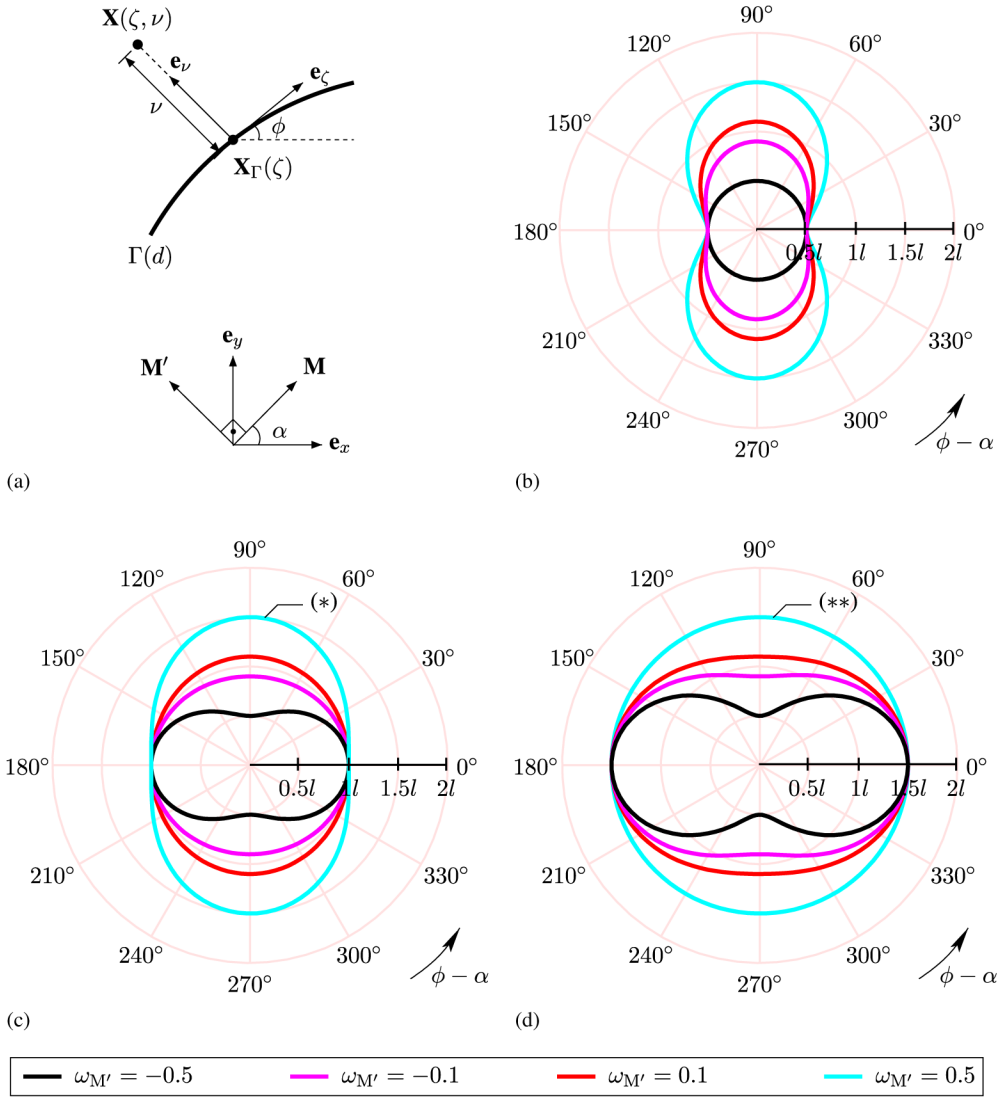

Fig. 4.

(a) Geometric profile of the sharp crack $\Gamma \in \mathcal{B}$ at point $\mathbf{X}_\Gamma(\zeta)$ together with the global and local coordinates systems (x, y) and (ζ, ν), respectively. Polar plots of the effective length scale parameter $l_e(\phi, a)$ shown for an orthotropic case ($\mathbf{M} \perp \mathbf{M}'$) in (17), with the anisotropy parameter (b) $\omega_M = -0.5$; (c) $\omega_M = 0.0$; (d) $\omega_M = 0.5$. The values assumed by the other anisotropy parameter $\omega_{M'}$ are shown in color (see the legend).

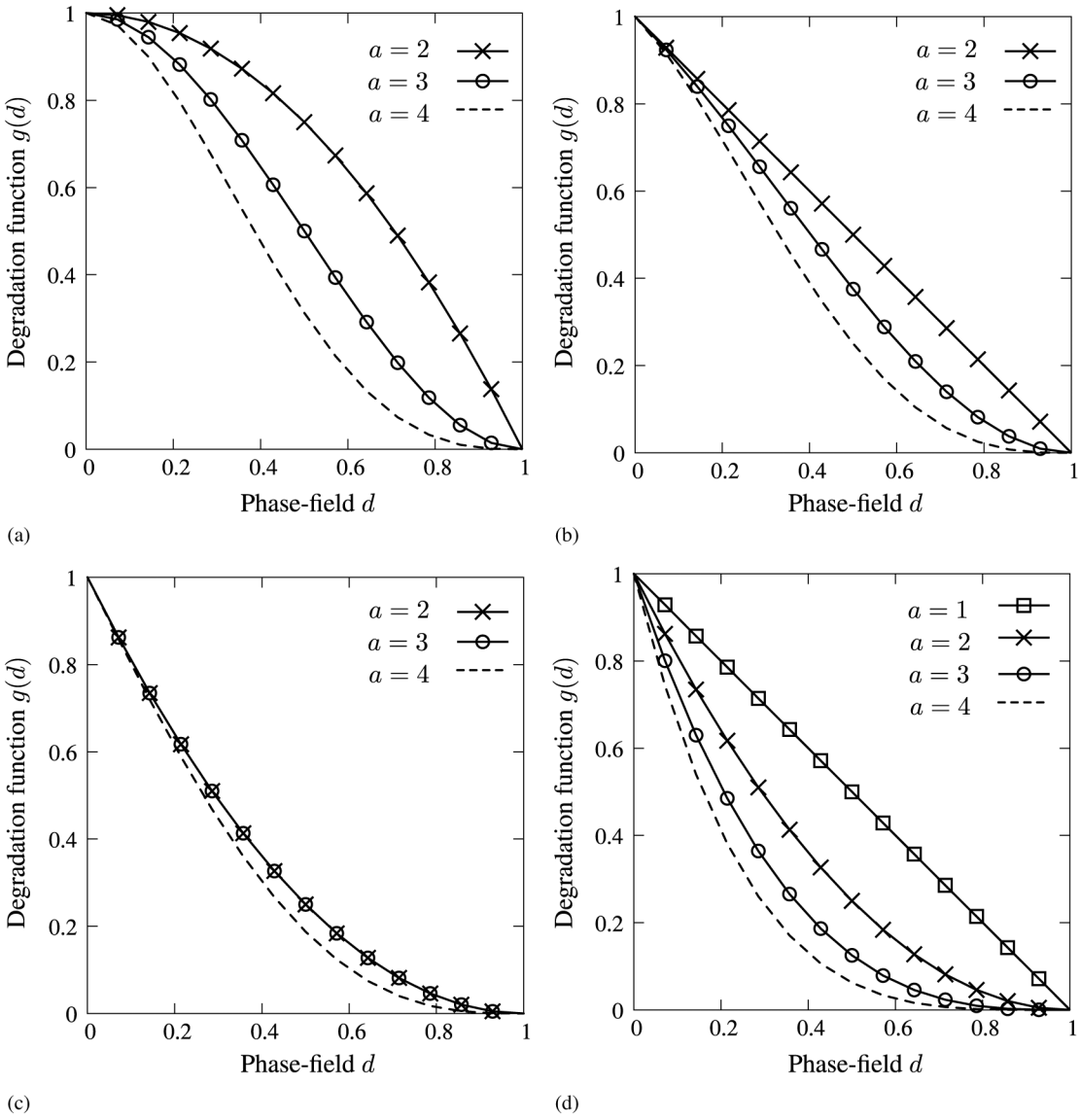

Fig. 5.

Qualitative behavior of the degradation function $g(d)$ vs d: (a) $b = 0$; (b) $b = 1$; (c) $b = 2$, according to (R2.1), while for (R2.2) $g(d)$ is stated in (d).

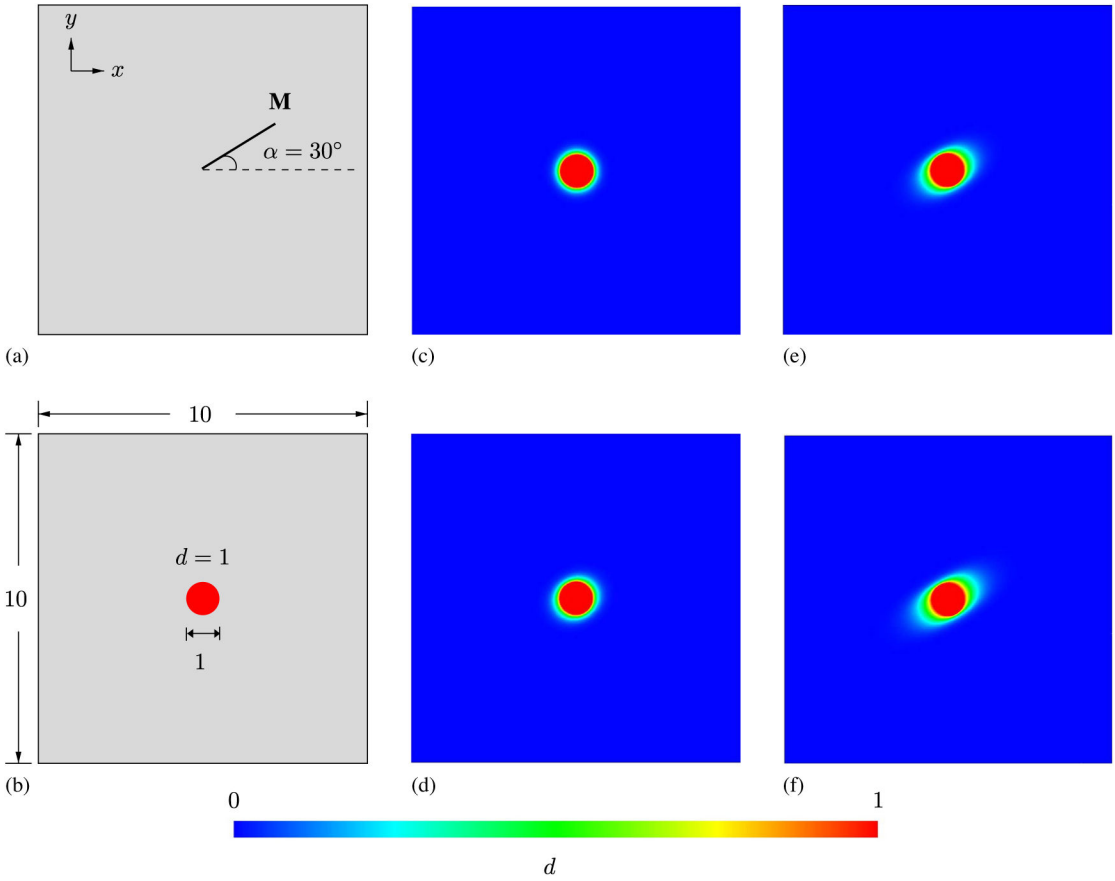

Fig. 6.

(a) 2-D square domain with one family of fibers oriented with an angle of $\alpha = 30°$ with respect to the x-axis; (b) geometry of the domain and boundary condition delineating a disc, where $d = 1$. Evolution of the phase-field parameter d for a varying anisotropy parameter ω_M: (c) 0; (d) 1; (e) 5, (f) 10. Dimensions are provided in millimeters.

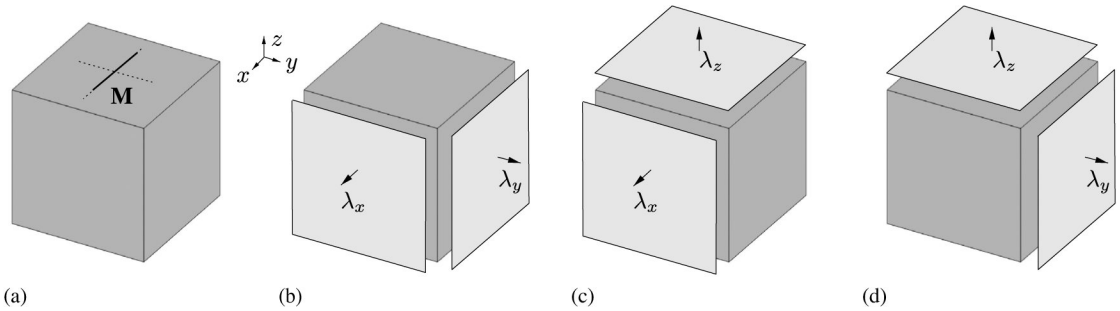

Fig. 7.

(a) Unit cube of a transversely isotropic tissue consisting of one family of fibers with the orientation **M** parallel to the *x*-direction, initially subjected to uniaxial deformations in the *x*-, *y*- and *z*-directions followed by a series of planar biaxial deformations (b) in the *xy*-plane; (c) in the *xz*-plane; (d) in the *yz*-plane.

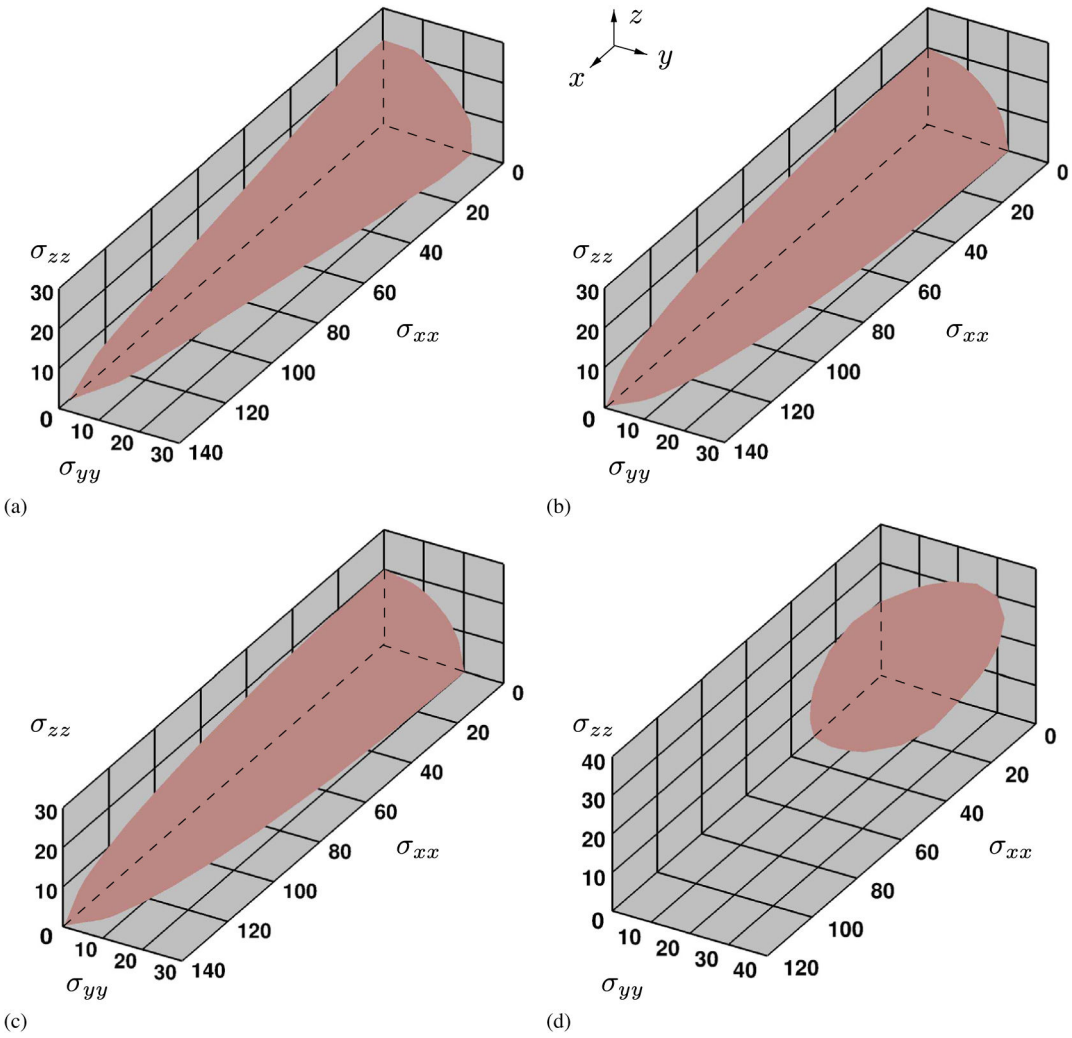

Fig. 8.

Failure surfaces in regard to Cauchy stresses σ_{xx}, σ_{yy} and σ_{zz} in kPa at which the failure conditions are satisfied, leading to $d > 0$ for (a) the energy-based; (b) the Tsai–Wu; (c) the maximum principal stress and (d) the Hill criterion.

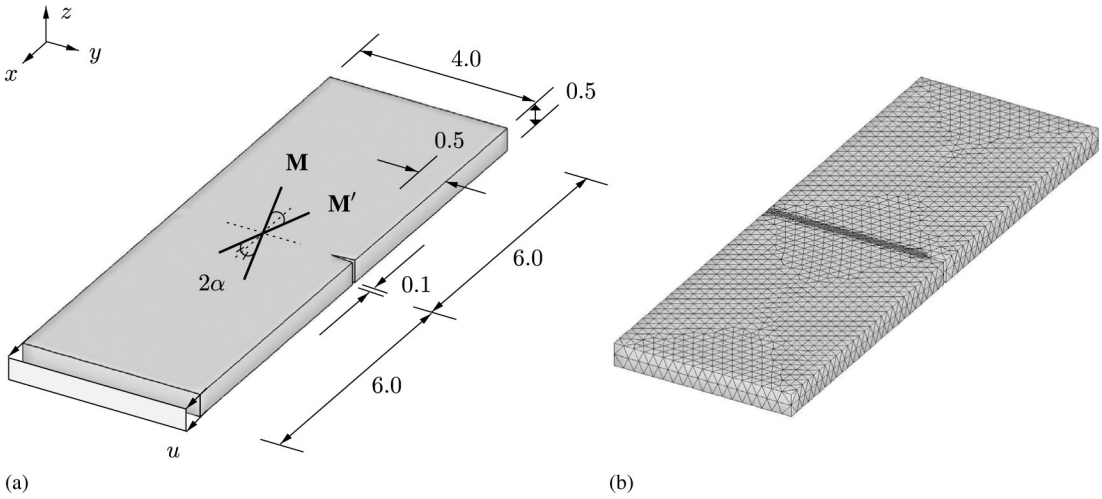

Fig. 9.

(a) Geometry of the strip with two families of fibers oriented in the directions **M** and **M′** and symmetrically arranged with respect to the x-axis by an angle α. The strip is uniaxially loaded by means of a displacement u; (b) finite element mesh of the corresponding geometry with refinement beyond the notch. Dimensions are provided in millimeters.

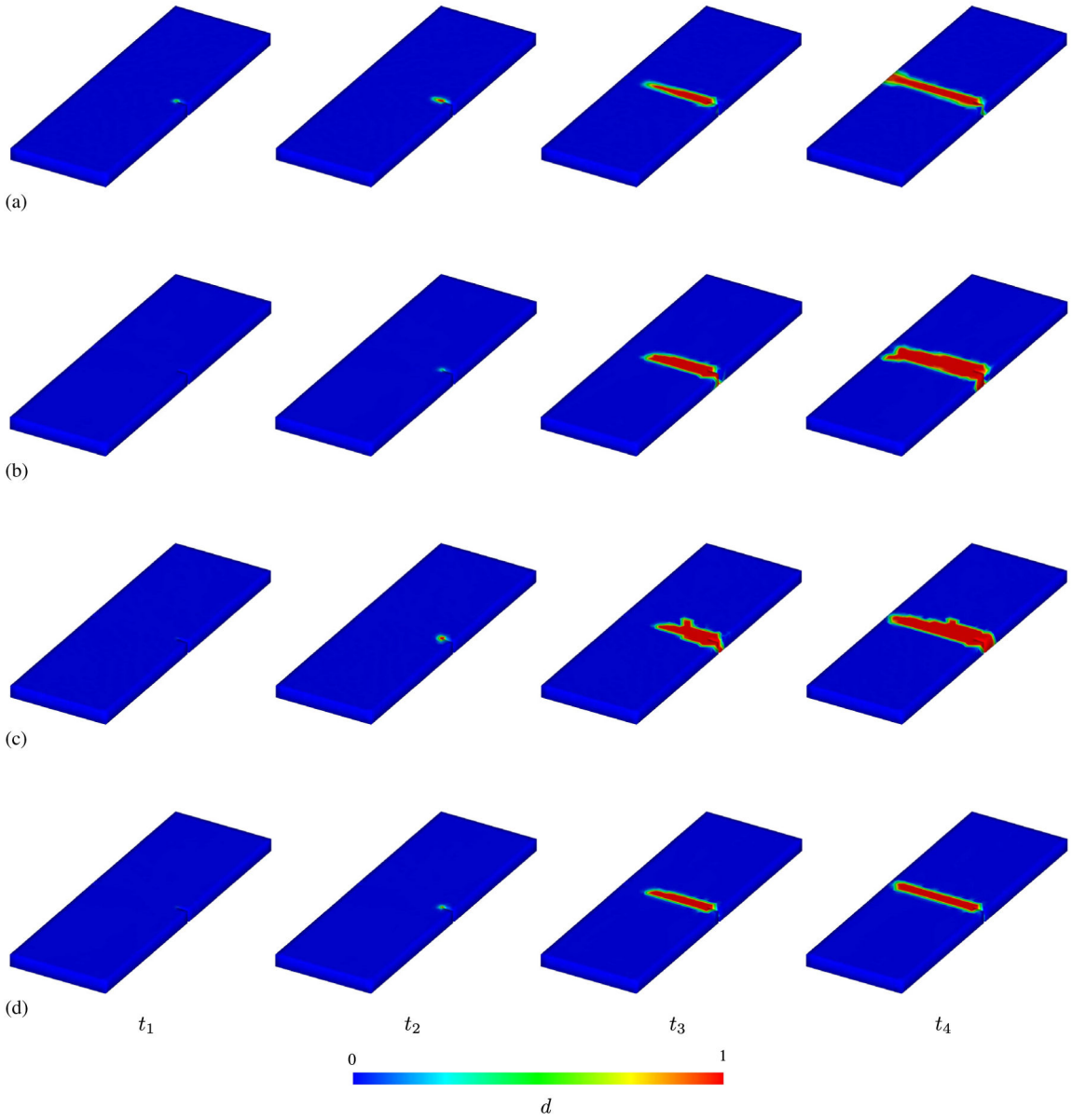

Fig. 10.

Evolution of the crack phase-field d in a notched strip of a hypothetical tissue uniaxially elongated: (a) energy-based criterion; (b) Tsai–Wu criterion; (c) principal stress criterion; (d) Hill criterion. The particular instants t_1, t_2, t_3 and t_4 manifest snapshots, compare with Fig. 11.

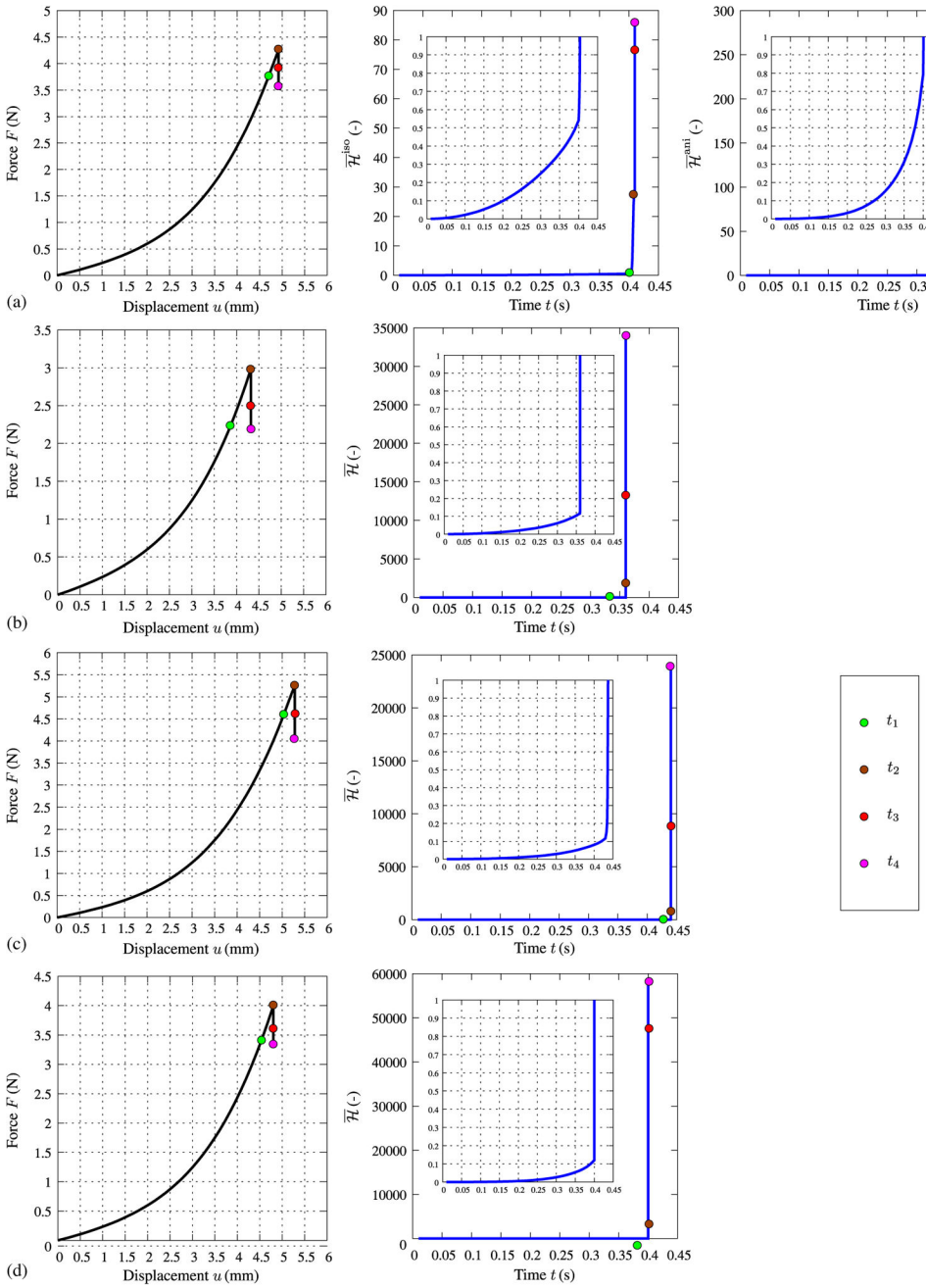

Fig. 11.

Plots corresponding to force F vs displacement u and to crack driving force $\overline{\mathscr{H}}$ vs time t, with regard to (a) energy-based criterion; (b) Tsai–Wu criterion; (c) principal stress criterion; (d) Hill criterion. The particular instants t_1, t_2, t_3 and t_4 manifest the snapshots in the previous figure (Fig. 10), and are also indicated here on curves. Zoom-in views for the $\overline{\mathscr{H}} - t$ curves are also shown.

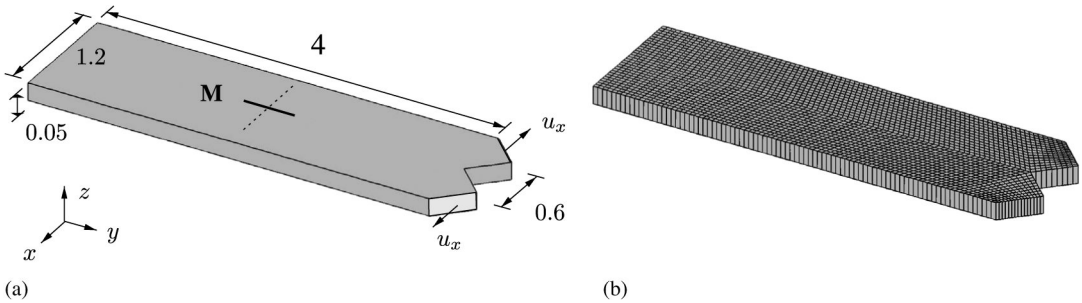

Fig. 12.

(a) Geometry of the strip with a single family of fibers with orientation **M** in the *y*-direction, corresponding to the collagenous component of the material. The strip is torn apart by means of a displacement u_x applied at the two arms in the positive and negative *x*-direction; (b) finite element mesh of the corresponding geometry. Dimensions are provided in millimeters.

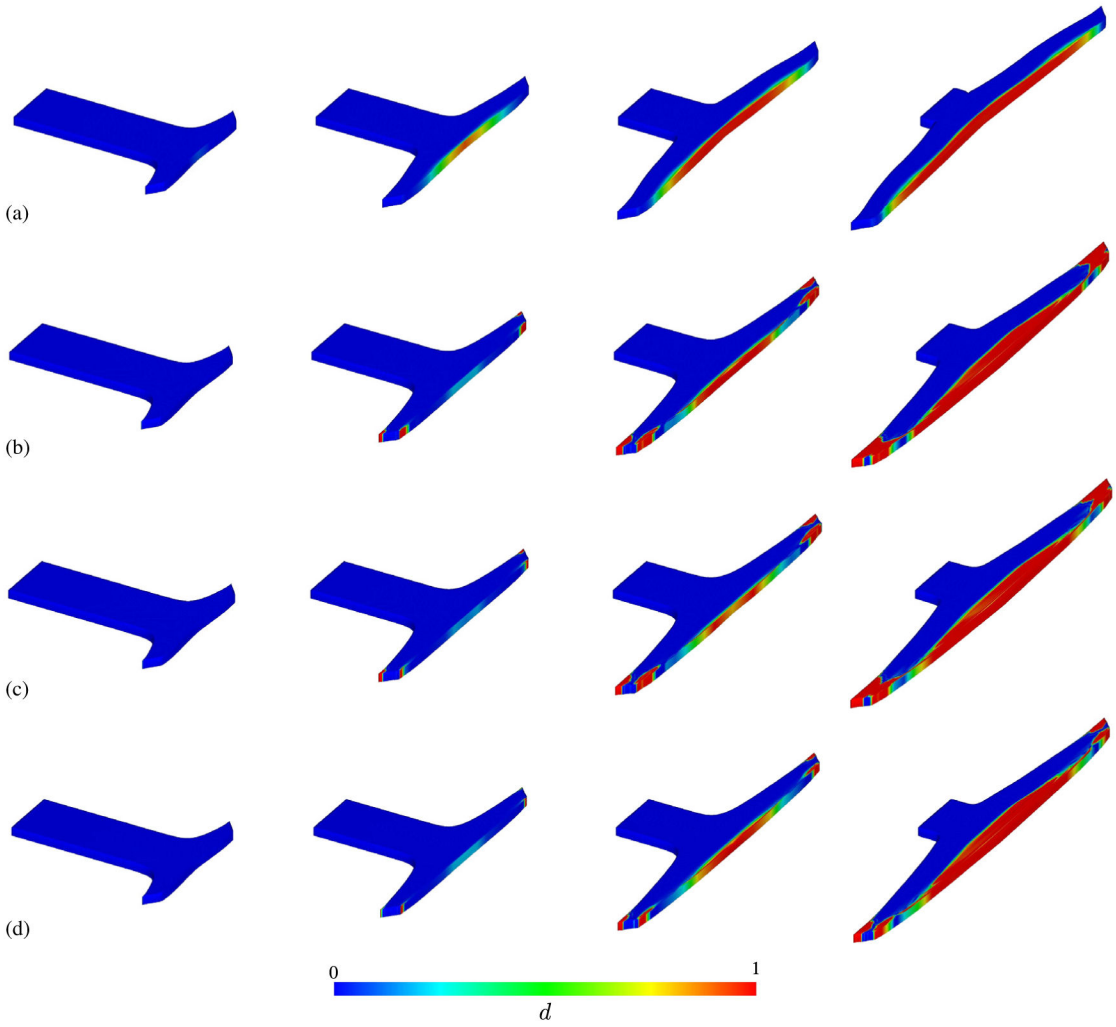

Fig. 13.

Evolution of the crack phase-field d for (a) the energy-based; (b) the Tsai–Wu; (c) the principal stress criterion; (d) the Hill criterion, as the arterial tissue with an initial tear is being pulled in two opposite directions.

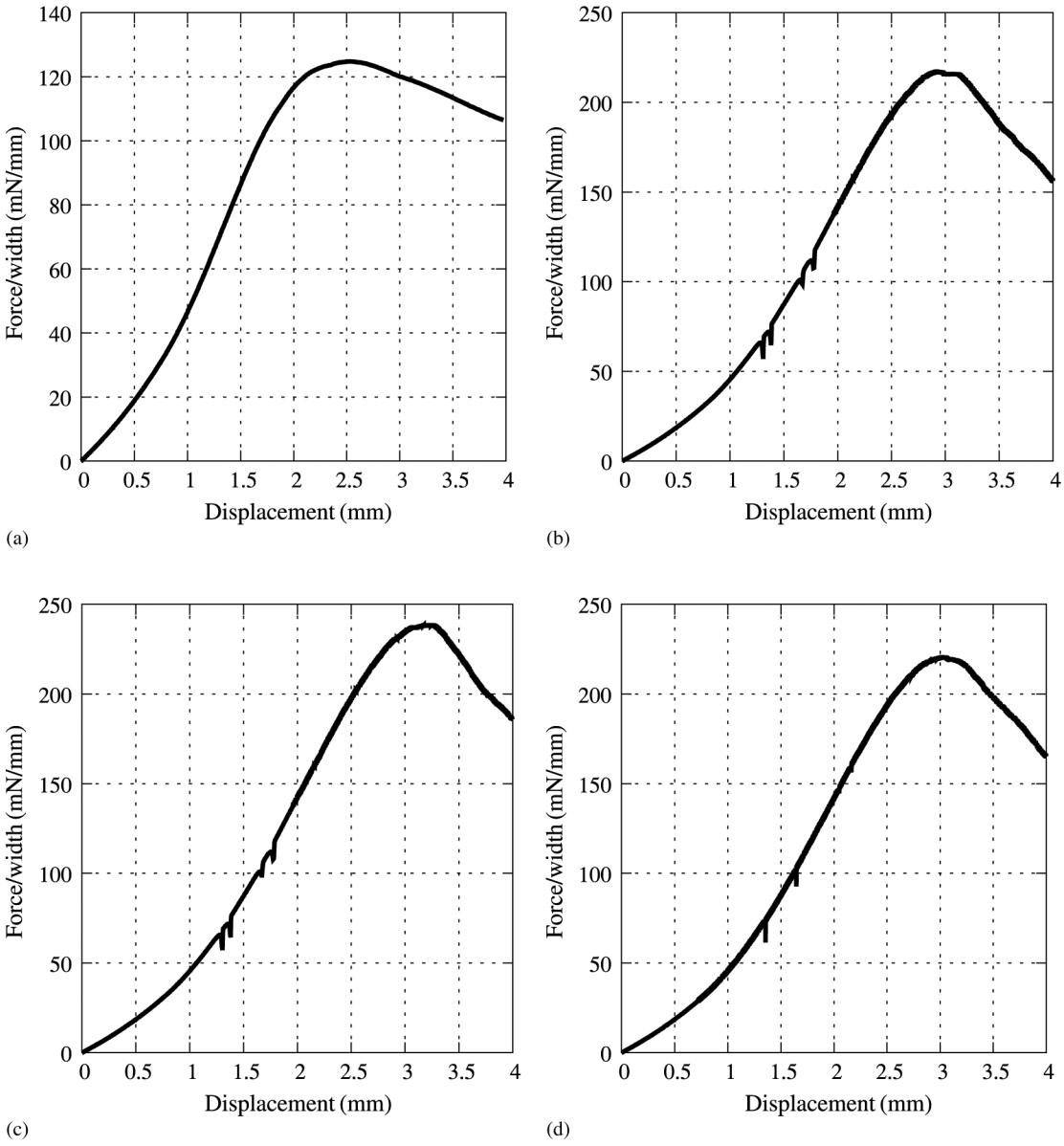

Fig. 14.

Plots of force per unit width for one arm against the applied displacement for (a) the energy-based; (b) the Tsai–Wu; (c) the principal stress criterion; (d) the Hill criterion.

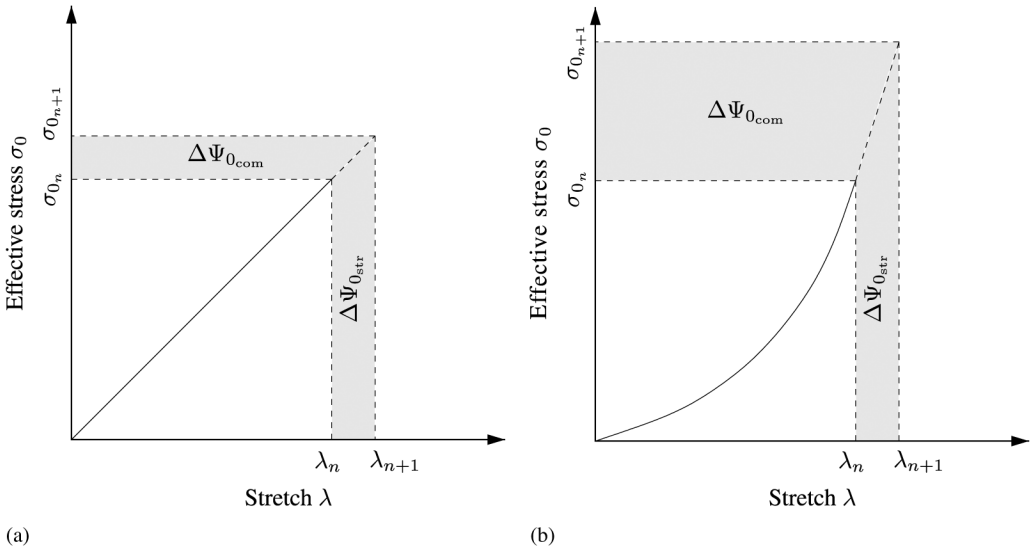

Fig. 15.

Qualitative sketch showing the relationship between the effective stress σ_0 and stretch λ, and the incremental change from $\sigma_{0_n} - \lambda_n$ to $\sigma_{0_{n+1}} - \lambda_{n+1}$ at a typical time step $\Delta t = t_{n+1} - t_n$:

(a) linear; (b) nonlinear material behavior with the corresponding changes in the effective complementary energy $\Delta\Psi_{0_{\text{com}}}$ and the effective strain energy $\Delta\Psi_{0\text{str}}$.

Table 1

Algorithm for the multi-field problem in $[t_n, t_{n+1}]$.

1. *Initialization*	-	At time t_n given: deformation map, phase-field, history field $\boldsymbol{\varphi}_n$, d_n, H_n
2. *Update*	-	Update the prescribed loads, $\tilde{\boldsymbol{\gamma}}$, $\overline{\boldsymbol{\varphi}}$ and $\tilde{\mathbf{t}}$ at current time $t_n{}_{+1}$
3. *Compute* $\boldsymbol{\varphi}_{n+1}$	-	Determine $\boldsymbol{\varphi}_{n+1}$ from the minimization problem of elasticity
$\mathrm{ALGO_M}$	•	$G^{\varphi} = \int_{\mathcal{B}} \left[\mathbf{g}\nabla_x(\delta\boldsymbol{\varphi}) : \boldsymbol{\tau}\right] \mathrm{d}V - \int_{\mathcal{B}} \delta\boldsymbol{\varphi} \cdot \rho_0 \tilde{\mathbf{y}} \mathrm{d}V - \int_{\partial\mathcal{B}} \delta\boldsymbol{\varphi} \cdot \tilde{\mathbf{t}} \mathrm{d}a = 0$
4. *Compute history*	-	Check crack initiation/propagation condition, update history
	•	$\mathscr{H}(t_{n+1}) \leftarrow \begin{cases} \mathscr{H}(t_n) & \text{if } \mathscr{H}(t_{n+1}) < \mathscr{H}(t_n) \\ \mathscr{H}(t_{n+1}) & \text{else} \end{cases}$
5. *Compute* d_{n+1}	-	Determine d_{n+1} from the minimization problem of crack topology
$\mathrm{ALGO_C}$	•	$G^{d} = \int_{\mathcal{B}} \delta d \left[d - 2(1-d)\mathscr{H} + \eta \frac{d - d_n}{\tau} \right] \mathrm{d}V + \int_{\mathcal{B}} \nabla(\delta d) \cdot \mathscr{L} \nabla d \mathrm{d}V = 0$

Table 2

Elastic material parameters and crack phase-field parameters for a transversely isotropic material, as studied in Section 5.2.

Elastic		$\mu = 10$ kPa	
		$k_1 = 20$ kPa	
		$k_2 = 1$	
Crack phase-field	Energy-based criterion	$g_c^{\text{iso}} = 5$ kPa mm	$g_c^{\text{ani}} = 15$ kPa mm
	Tsai-Wu criterion	$\sigma_x^u = 140$ kPa	$\sigma_y^u = \sigma_z^u = 20$ kPa
	Principal stress criterion	$\sigma_{\text{crit}} = 140$ kPa	$\mathfrak{a}_2 = 1, \mathfrak{a}_2 = \mathfrak{a}_3 = 7$
	Hill criterion	$\sigma_x^{\mathfrak{u}} = 30$ kPa	$\sigma_y^u = \sigma_z^u = 20$ kPa

Table 3

Elastic material parameters and crack phase-field parameters for a strip extended uniaxially, as studied in Section 5.3.

Elastic		$\kappa = 10^4$ kPa	
		$\mu = 16.95$ kPa	
		$k_1 = 243.57$ kPa	
		$k_2 = 2.57$	
		$\alpha = 44.5°$	
Crack phase-field	Energy-based criterion	$g_c^{\text{iso}} = 1$ kPa mm	$g_c^{\text{ani}} = 1.5$ kPa mm
	Tsai-Wu criterion	$\sigma_x^u = \sigma_y^u = 1000$ kPa	$\sigma_z^u = 333$ kPa
	Principal stress criterion	$\sigma_{\text{crit}} = 1000$ kPa	$\mathfrak{a}_1 = \mathfrak{a}_2 = 1, \mathfrak{a}_3 = 3$
	Hill criterion	$\sigma_x^u = \sigma_y^u = 1000$ kPa	$\sigma_z^u = 333$ kPa

Table 4

Number of steps times step sizes considered to simulate the uniaxial extension test for four different failure criteria.

Energy-based criterion	40×10^{-2}	10×10^{-3}	55×10^{-6}	
Tsai-Wu criterion	36×10^{-2}	10×10^{-5}	129×10^{-8}	
Principal stress criterion	43×10^{-2}	10×10^{-3}	10×10^{-6}	172×10^{-10}
Hill criterion	40×10^{-2}	5×10^{-5}	157×10^{-8}	

Table 5

Crack phase-field parameters for a transversely isotropic strip peeled off as studied in Section 5.4.

Crack phase-field	Energy-based criterion	$g_c^{\text{iso}} = 4.17$ kPa mm	$g_c^{\text{ani}} = 12.5$ kPa mm
	Tsai-Wu criterion	$\sigma_y^{\text{u}} = 2500$ kPa	$\sigma_x^{\text{u}} = \sigma_z^{\text{u}} = 500$ kPa
	Principal stress criterion	$\sigma_{\text{crit}} = 2500$ kPa	$\mathfrak{a}_2 = 1, \quad \mathfrak{a}_1 = \mathfrak{a}_3 = 5$
	Hill criterion	$\sigma_y^{\text{u}} = 2500$ kPa	$\sigma_x^{\text{u}} = \sigma_z^{\text{u}} = 500$ kPa

Table 6

Number of steps times step sizes considered to simulate the peel test with four different failure criteria.

Energy-based criterion	1000×10^{-3}	
Tsai-Wu criterion	490×10^{-3}	5100×10^{-4}
Principal stress criterion	490×10^{-3}	5100×10^{-4}
Hill criterion	180×10^{-3}	8200×10^{-4}